

Elongation of a Solar Filament and its Three-Dimensional Numerical Reconstruction for Magnetic Structures

GARIMA KARKI,¹ JINHAN GUO*,^{2,3} BRIGITTE SCHMIEDER,^{3,4,5,6} RAMESH CHANDRA,¹ PASCAL DÉMOULIN,⁴ STEFAAN POEDTS,^{3,7} AND BERNARD GELLY⁸

¹Department of Physics, DSB Campus, Kumaun University, Nainital – 263001, India

²School of Astronomy and Space Science and Key Laboratory of Modern Astronomy and Astrophysics, Nanjing University, Nanjing 210023, People's Republic of China

³Centre for mathematical Plasma Astrophysics, Dept. of Mathematics, KU Leuven, 3001 Leuven, Belgium

⁴LIRA, Observatoire de Paris, Université PSL, UMR8254 (CNRS), Sorbonne Université, Université Paris Cité, 5 place Jules Janssen, 92195 Meudon, France

⁵SUPA, School of Physics & Astronomy, University of Glasgow, Glasgow G12 8QQ, UK

⁶LUNEX EMMESI COSPAR-PEX Eurospacehub, Kapteyn straat 1, Noordwijk 22001 BB Netherlands

⁷Institute of Physics, University of Maria Curie-Skłodowska, Lublin, Poland

⁸THEMIS, Canary Islands, ES

ABSTRACT

Quiescent filaments are prominent features of the solar atmosphere, and their evolution reflects the coronal magnetic field's response to photospheric magnetic activity. Here, we report on a quiescent filament observed from 2023 September 28–29, aiming to understand how the magnetic configuration shapes its feet and drives its extension. For this purpose, high-resolution spectral data in H α and Mg II k are used from the Télescope Héliographique pour l'Etude du Magnétisme et des Instabilités Solaires (THEMIS) and the Interface Region Imaging Spectrograph (IRIS), respectively. To track changes in the filament, we utilise long-term data from the Atmospheric Imaging Assembly (AIA) on the Solar Dynamics Observatory (SDO) and from the Global Oscillation Network Group (GONG). We analyse the longitudinal magnetic field in the photosphere using the Solar Optical Telescope (SOT) onboard Hinode, as well as SDO/Helioseismic and Magnetic Imager (HMI) data. In addition to this, we use GONG H α data to analyze the longitudinal oscillations in the filament. Observations show that parasitic polarities and canceling flux play a key role in forming and reorganizing the filament feet and in lengthening the filament. A 3D MHD reconstruction using vector magnetograms reveals that its magnetic configuration evolves into a full flux rope (FR), whose extension on the second day matches the observed filament growth. The FR is separated from the surrounding nearly potential field by quasi-separatrix layers, which in turn are separated by current layers. They get more organized around the FR as it is growing up. Moreover, the longitudinal oscillations in the extended filament are attributed to heating from flux cancellation in underlying bright points.

Keywords: Prominences, Quiescent; Prominences Magnetic Field; Spectral Line; Velocity Fields; MHD

1. INTRODUCTION

1.1. Formation of filaments

Solar filaments (known as prominences at the solar limb) are relatively cold (10^4 K) and dense plasma embedded in the hot corona (10^6 K, E. Tandberg-Hanssen 1974, 1995; N. Labrosse et al. 2010; D. H. Mackay et al. 2010). Filament fine structures are composed of thin and dark fibrils (Y. Lin et al. 2005; G. Karki et al. 2025). The main thin

structure running along the filament is called the spine. This is typically understood as the top part of the filament. Lateral extensions of fibrils are typically present on both sides of the filament, forming a global structure known as feet or barbs. All the filament fibrils are slightly inclined with respect to the polarity inversion line (PIL). In magnetic structures, including magnetic dips such as the flux rope (FR) and the sheared arcade, the dense plasma is supported against gravity by the Lorentz force.

It is important to understand filament formation because filament eruptions are frequently associated with the onset of coronal mass ejections (CMEs). Filament first starts to rise slowly (R. Chandra et al. 2021; P. Devi et al. 2021; X. Cheng et al. 2020), then evolves to erupt through kink, torus instability and fast magnetic reconnection (B. Kliem & T. Török 2006a,b; G. Aulanier et al. 2010; C. Jiang et al. 2021; C. Xing et al. 2024). Depending on the environment of the FR, it can escape and accelerate particles in open magnetic field lines or be confined if the magnetic field strength is too strong above the FR (T. Amari et al. 2018), or if the Lorentz force leads to an increase in the electric current, forcing the FR to rotate and ultimately stop its rising phase (X. M. Zhang et al. 2024; J. H. Guo et al. 2024a). During an eruption, the FR is expelled and evolves into a CME. When a CME carrying a negative (southward) B_z component reaches Earth's environment, it induces magnetic reconnection within Earth's intricate magnetosphere, triggering geomagnetic storms.

There are various models for forming a filament, such as injection, levitation, and (or) evaporation-condensation (D. H. Mackay et al. 2010; Y. Zhou 2025; R. Keppens et al. 2025). The injection model is more relevant for active region (AR) filaments, and the levitation model is relatively well accepted when chromosphere fibrils gather together and rise. Nevertheless, the evaporation-condensation model is, to date, the best accepted. Many hydrodynamic (HD) or magnetohydrodynamic (MHD) simulations of filament formation have been developed around this idea (J. T. Karpen et al. 2003, 2006; C. Xia et al. 2011, 2014; Y.-H. Zhou et al. 2014; Y. H. Zhou et al. 2020; J. H. Guo et al. 2021b; V. Liakh & J. Jenkins 2025). Extensive studies have been performed theoretically on the dips present in an FR to characterize parameters such as the dip depth, the dip extension along the main axis, and the number of dips (C. R. DeVore et al. 2005; Y.-H. Zhou et al. 2017; J. H. Guo et al. 2021b, 2022). It was concluded that magnetically connected threads due to multiple dips are more likely to exist in quiescent filaments than in AR filaments (J. H. Guo et al. 2021b).

1.2. Magnetic configuration of filaments

Filaments are classified as AR filaments when present inside an AR, quiescent filaments when located in the quiet Sun (typically at high latitudes), and intermediate filaments when they lie between two ARs or have one foot rooted within an AR. They are commonly modeled as sheared arcades or twisted flux ropes (G. Aulanier & P. Démoulin 1998; P. F. Chen et al. 2014; Y. Ouyang et al. 2017), with approximately 90% of filaments supported by twisted flux ropes (Y. Ouyang et al. 2017). In particular, even a filament might be supported by an FR in one segment and by a sheared arcade (Y. Guo et al. 2010; H. Li et al. 2025). It has been demonstrated that large twists are present in quiescent filaments, leading to the formation of short threads, while in AR filaments, there are longer threads (J. H. Guo et al. 2021b, 2022). Nowadays, data-driven simulations demonstrate the formation of FRs as the AR evolves with shearing motions and moving polarities (C. Jiang et al. 2021; J. H. Guo et al. 2024b; B. Schmieder et al. 2024; W. Wang et al. 2025; H. Li et al. 2025). The evolution of photospheric magnetograms is crucial for understanding filament formation and evolution.

1.3. Magnetic Barbs / Feet

Filaments are located between two inverse photospheric magnetic polarities separated by the polarity inversion line (PIL). Viewed on the limb, filaments/prominences are attached to the disk by regularly spaced legs or feet. Viewed on the disk, the feet are also called barbs (S. F. Martin et al. 1992). In this paper, we will preferentially use the word feet. Commonly, feet are related to parasitic magnetic polarities, which have the opposite sign from the dominant magnetic polarity on each side of the PIL. Feet shape and existence depend on the location and magnetic flux of the parasitic polarities (G. Aulanier et al. 2000). Feet are located on magnetic field lines that bend towards the photosphere, where they are attracted by parasitic polarities. Then, the magnetic field lines present dips, away from the main filament body, where cool plasma can be trapped (G. Aulanier & P. Démoulin 1998; G. Aulanier et al. 1999).

Some magnetic field lines with dips extend to the photosphere in the filament channel, forming feet. Plasma in feet does not drain back to the photosphere, unlike at the filament ends (e.g., B. Schmieder et al. 1985; J. H. Guo et al. 2021b). Any motion of photospheric granules and supergranules affects the dynamics of the filament. Supergranules

are well identified in the chromosphere (B. Schmieder et al. 2014; C. Zhou et al. 2021). In B. Schmieder et al. (2024), converging flows were identified around H α filament feet and at the edges of the EUV filament channel, which is wider than the H α channel (G. Aulanier & B. Schmieder 2002). The horizontal photospheric velocity may reach 1 km s $^{-1}$. In some locations, horizontal flows crossing the channel are observed, which eventually indicate large-scale shearing (B. Schmieder et al. 2014).

The existence of parasitic polarities forming barbs or feet remains controversial (A. A. van Ballegooijen 2004; Q. Liu & C. Xia 2022; H. Chen et al. 2025). The existence of dips cannot be directly proven by observation. J. Dudík et al. (2008) studied the topological departures from translational invariance along a filament. They calculated the coronal magnetic field from a “linear magnetohydrostatic” extrapolation of a composite magnetogram and detailed the shape of the dips corresponding to a long observed filament and their feet. They showed the importance of the network at the border of filament for the split topology in the filament. Other types of barbs/feet have been recently described as follows: dynamic barbs due to the longitudinal oscillations of some threads (Y. Ouyang et al. 2020), and barbs due to the indented threads (P.-F. Chen et al. 2020; J. H. Guo et al. 2022). These barbs do not correspond to any prominence footpoint. Below, we use the term ‘barb’ to refer only to dynamic lateral extensions, while ‘feet’ is reserved for the most stationary lateral/downward extensions, which still evolve but on long timescales (hours, days) relative to the photospheric field.

Filament feet and spines resemble an accumulation of parallel, short threads (G. Karki et al. 2025). These short threads can be formed by the cooling of plasma in coronal loops (J. T. Karpen et al. 2006; M. Luna et al. 2012). They can also form by merging adjacent chromospheric fibrils due to strong shear (R. Joshi et al. 2022). In that paper, they conjectured that the squeezed fibrils were rising and forming a longer filament. Such filament formation has been proposed recently using MHD numerical simulations of supergranules (H. Chen et al. 2025). In this case, prominence material, including feet, remains in the dip of the helical field lines, which are piled up vertically from the photosphere to the spine.

1.4. Chirality

Feet/barbs indicate the chirality of the filament. If they are inclined like the highway exits in the European mainland, they are right-bearing filaments (S. F. Martin et al. 1992; E. Tandberg-Hanssen 1995; A. López Ariste et al. 2006; P. F. Chen et al. 2014; P.-F. Chen et al. 2020). In contrast, if the feet/barbs organisation is the mirror view, they are left-bearing filaments. Another filament chirality is defined by the direction of the axial magnetic field. For an observer located on the positive-polarity side of the PIL, the configuration is called dextral if the axial magnetic field points to the right, and sinistral if it points towards the left. S. F. Martin (1998) found a correlation between these two types of chirality, i.e., left-bearing/right-bearing feet correspond to sinistral/dextral filaments. For FR models, such correlation naturally arises from the positive/negative magnetic helicity of the FR (G. Aulanier & P. Démoulin 1998).

Magnetic arcade above the FR is expected to have the same helicity sign (since the FR is formed by the reconnection of part of this arcade). Then, the coronal arcade above the filament is expected to be right- or left-skewed, respectively, as typically observed (see D. H. Mackay et al. 2010, for a more comprehensive review). The ARs with a preponderance of positive/negative helicity are in the southern/northern hemisphere (Y. Ouyang et al. 2017). Moreover, cases have been reported where dextral and sinistral filaments coexist in the same hemisphere (R. Chandra et al. 2010; Y. Ouyang et al. 2017).

1.5. Large amplitude Oscillations

Observations of large-amplitude oscillations in filaments, defined by a velocity greater than 10 km s $^{-1}$, are frequent nowadays (see the review of I. Arregui et al. 2018). The detection of these oscillations is possible because of the regular, long-time interval observations provided by space- and ground-based instruments. The triggers are various (M. Luna et al. 2018). They can be due to Moreton or EUV waves (A. Asai et al. 2012; P. Devi et al. 2022), shock waves (Y. Shen et al. 2014; V. Jerčić et al. 2022), nearby jets (R. Joshi et al. 2023), subflares and flares or related to the eruptive phase of a filament (K. Bocchialini et al. 2011). M. Luna et al. (2018) analyzed the oscillations detected in 196 filaments observed with GONG. Nearly half of them have a large amplitude velocity ($v > 10$ km s $^{-1}$). The flow direction makes an angle of about 20 degrees relative to the filament spine. Considering that fine structures of filament trace the local supporting magnetic field lines, they deduced that the flow was along the strands of the filament and, therefore, it should be longitudinal oscillations. The average period was 58 ± 15 min.

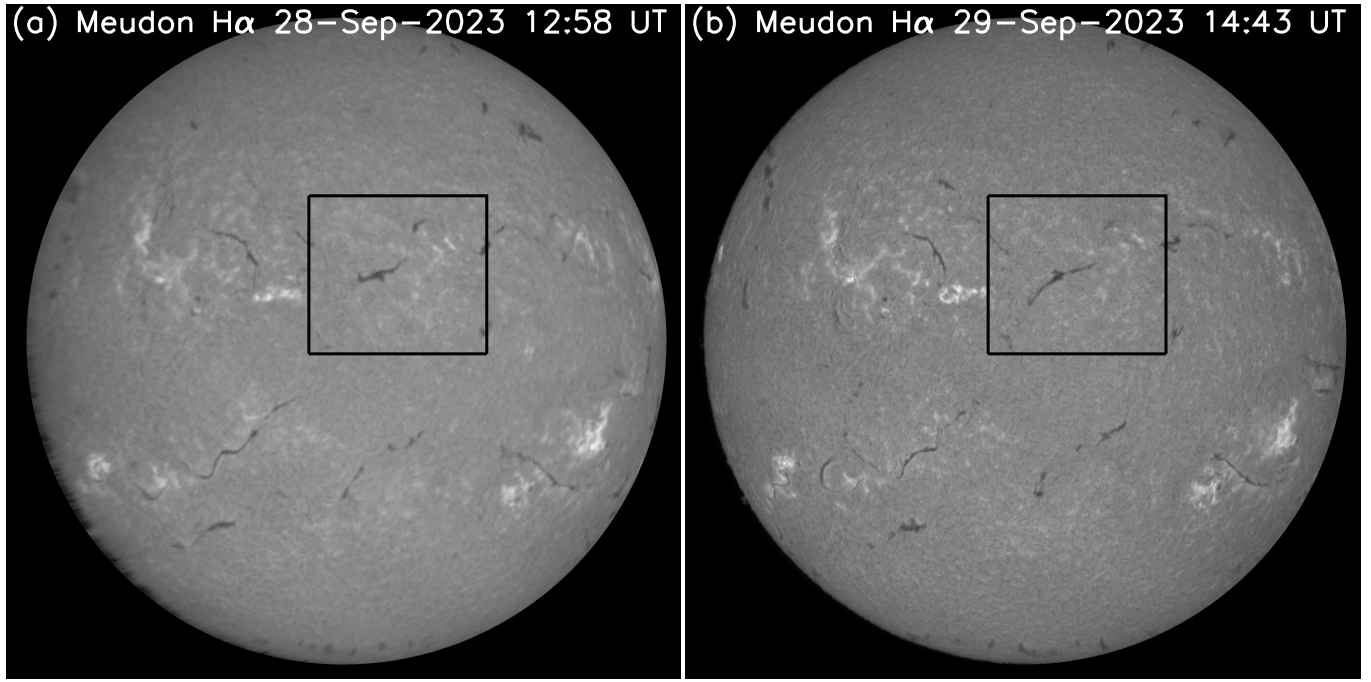


Figure 1. Panels (a) and (b) show the full disk H α image observed by Meudon spectroheliograph on 28 and 29 September 2023, respectively. The black box indicates the filament observed by THEMIS and IRIS during the 2023 campaign. We note the change in shape of the east end of the filament on September 29.

The prominence oscillatory periods depend on height, with periods increasing by up to 10-15 min for a rise in height of approximately 30-40 Mm (J. Hershaw et al. 2011). Damping of the oscillations is also observed in many studies (Y. Bi et al. 2014). In their observations, the oscillation period increased from 60 min to 90 min after two oscillation periods. They suggest that the curvature of magnetic fields supporting the filament becomes flatter during the evolution phase, leading to longer oscillation periods.

Transverse and longitudinal oscillations could coexist in many cases (R. Mazumder et al. 2020; S. Tan et al. 2023). The observed velocity profiles are typically fitted with an exponentially decaying sine function. This allows the estimation of wave periods, damping times, and initial amplitudes.

The theoretical model of M. Luna et al. (2012) for the large amplitude oscillations suggests the following scenario: after an energetic event (a subflare, for instance) occurring close to a filament, the injected energy evaporates plasma at the flux tube footpoint closest to the energetic event. Then, the upward flow of hot plasma pushes the cold plasma condensations (threads) located in the dips of the magnetic structure, and longitudinal oscillations start. The oscillations are gravity-driven, with the restoring force being the projected solar gravity along magnetic field lines. More generally, several theoretical models are based on pendulum models with adaptations that take into account the source and possible wave reflections (M. Luna et al. 2012; V. Jerčić et al. 2022). The damping time depends on the curvature of the dips and the altitude. It may also be affected by multi-threads that reconnect (Y.-H. Zhou et al. 2017).

1.6. Aim and outline of the paper

The goal of this paper is to understand the formation of the feet and the elongation of a filament observed during two days. We used multi-wavelength observations of a quiescent filament obtained with ground-based and space-based instruments (Section 2.1 and Appendix). In Section 2, we describe the morphology of the filament and its magnetic environment. In Section 3, we reconstruct their 3D magnetic structures with the non-linear-force-free-field (NLFFF) extrapolation. Section 4 presents the conclusion.

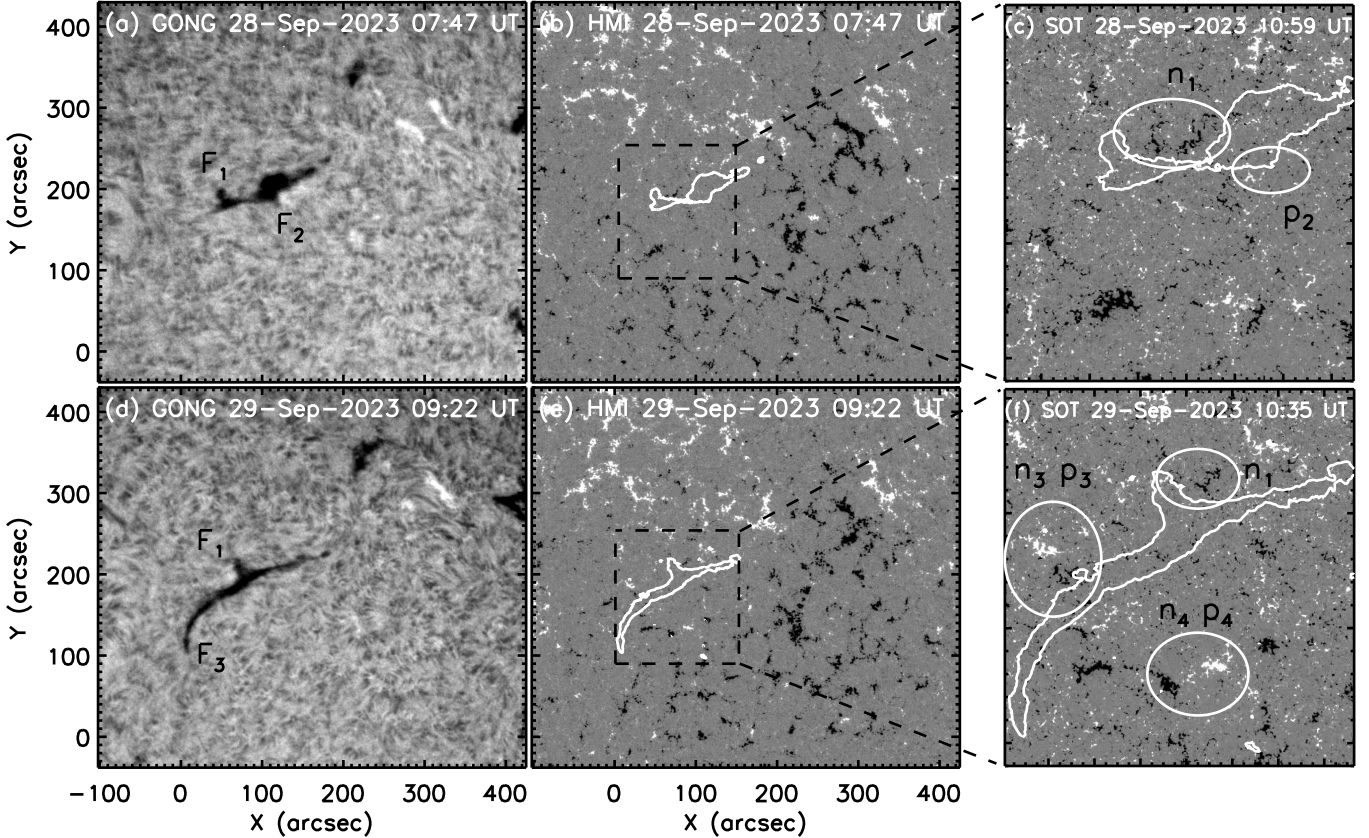


Figure 2. Zoom on the filament observed with GONG H α (panels a and d), the longitudinal magnetic field (HMI in panels b and e) and a local zoom of Hinode/SOT with levels ± 100 G (in panels c and f) for September 28 and September 29. The two FOVs of the filament are aligned with the FOV of 29 Sept at 11:00 UT. We note that the global pattern of the network polarities of HMI is well co-aligned. The FOV of SOT is represented by the dashed black box in HMI magnetograms. F₁, F₂, and F₃ are feet of the filament. On September 28, two feet, F₁ and F₂, are observed, while on September 29, feet F₁ and the extension F₃ are present. In the SOT maps, ovals indicate the parasitic polarities (n₁, p₂) and cancelling flux regions (n₃ p₃, n₄ p₄). More details on the observed data sets, including the observed wavelengths, are provided in the Appendix A. An animation of panels a and d is available, starting on 27 September 2023 at 23:59 UT and ending on 29 September 2023 at 23:58 UT. The real-time duration of the animation is 3 min 12 s. (An animation of this figure is available in the online article.)

2. FILAMENT OBSERVATIONS

2.1. *Alignment of the data*

The filament that we choose to analyse is a quiescent filament on the solar disk observed for 2 days, 28–29 September 2023, using the following space- and ground-based observatories (see the full description of the instruments in the Appendix): the Solar Dynamics Observatory (SDO; [W. D. Pesnell et al. 2012](#)), the Interface Region Imaging Spectrograph (IRIS; [B. De Pontieu et al. 2014](#)), the Hinode/Solar Optical Telescope (Hinode/SOT; [S. Tsuneta et al. 2008](#)), the Global Oscillation Network Group (GONG; [J. W. Harvey et al. 1996](#)), the Télescope Héliographique pour l’Etude du Magnétisme et des Instabilités Solaires (THEMIS; [P. Mein & J. Rayrole 1985](#)). We focus on the evolution of this filament because it was the target of the THEMIS and IRIS observation campaign and was observed with these two high-spatial resolution instruments ([B. Schmieder et al. 2025](#); [B. De Pontieu et al. 2014](#)).

The THEMIS observations acquired with a small pixel size of 0.06'' along the slit have been described for September 29 in a previous paper ([G. Karki et al. 2025](#)). The data from September 28 were acquired in a similar manner between 08:23 UT and 11:19 UT with the scans numbered t01 to t20. They consist of observations of different sections of the filament taken irregularly over time. Some of them (e.g., t019; THEMIS observation file at 11:10 UT) were carried out with accumulation (10×200 ms = 2 s), a step size of 0.5'', covering a span of $\pm 40''$, and a slit length ranging between 110 – 120''. Some of the spectra are very good during each scan, particularly between 10:10 UT and 11:19

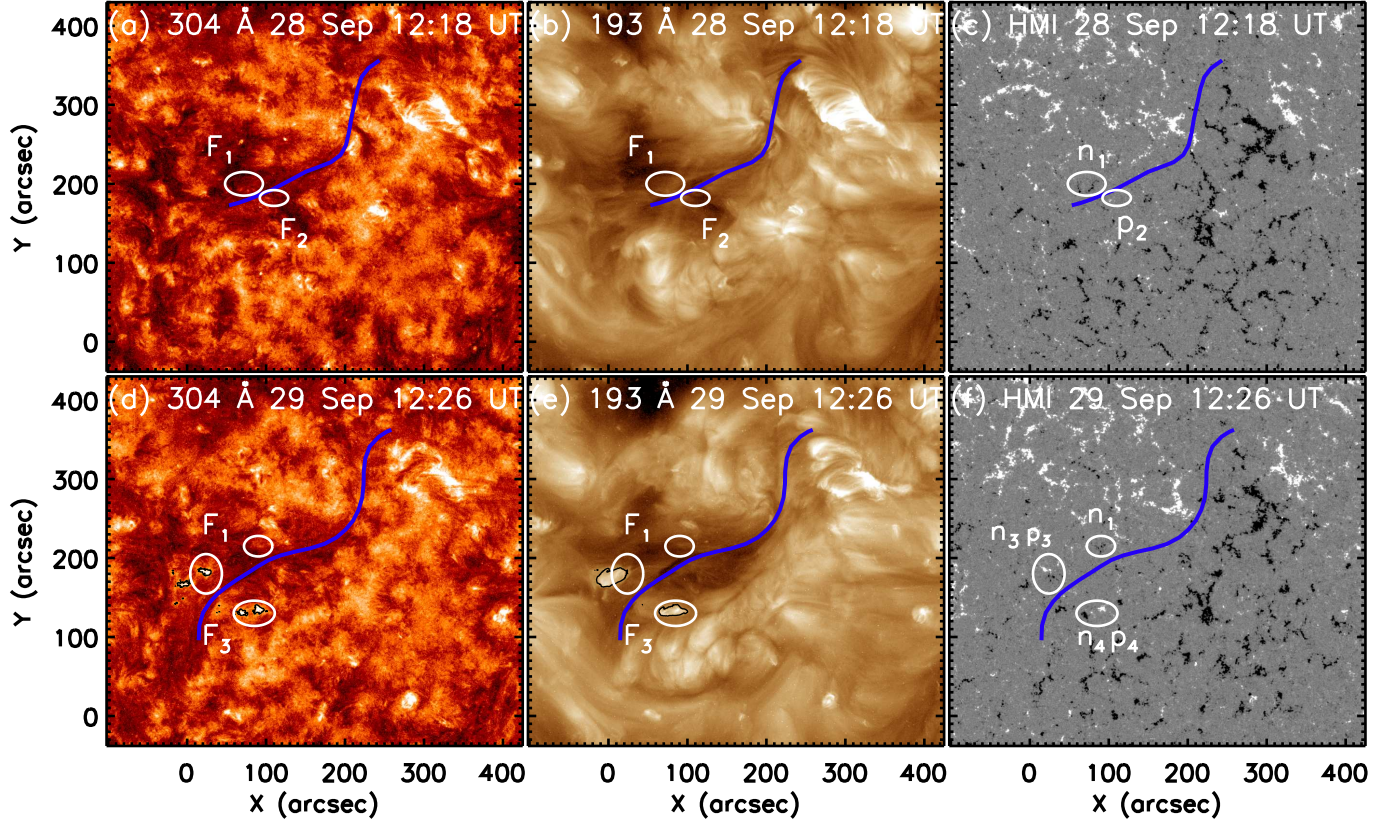


Figure 3. Region of the filament observed in AIA 304 and 193 Å on the 28th and 29th September 2023 (panels a, d and b, e, respectively). The FOVs are aligned on the FOV of September 29 at 11:00 UT. HMI magnetograms with levels ± 100 G of the filament region for September 28 and 29 are shown in panels (c) and (f), respectively. The blue curve represents the filament spine traced along the dark part of the filament from AIA 193 Å images for the 28th and 29th of September, respectively. The feet F_1 , F_2 , and the extension F_3 are indicated in panels a, b, d, and e. The polarities n_1 , p_2 are indicated in panel c, and n_3 , p_3 , n_4 , p_4 in panel f. The ellipses marked in the AIA filter images correspond to those in the HMI magnetograms, denoting the parasitic polarities (n_1 , p_2) and the dipoles (n_3 – p_3 and n_4 – p_4). The black contours in panels d and e outline the observed EUV bright points. An animation of this figure is available, starting at 00:00 UT on 28 September and ending at 23:57 UT on 29 September. The real-time duration of the animation is 32 s. (An animation of this figure is available in the online article.)

UT (three images: 10:38 UT, 11:10 UT, and 11:19 UT), but the reconstructed images are not homogeneous due to the rapid changes in seeing, which are corrected by the adaptive optics.

The Meudon spectroheliograph in the H α wavelength is used to study the global structure of the filament. The observations are obtained by scanning the full disk in one minute with an image scale of 1''.1/pixel.

All data sets for September 28 and 29 are aligned to a common reference time (September 29, 2023, at 11:00:00 UT) to facilitate a comparative analysis between the two days with range [-102, 425] arcsec in x and [-38, 430] arcsec in y. Observations from SDO, GONG, and Meudon were corrected for the solar differential rotation using the drot_map routine available in SolarSoft system (SSW). Residual misalignments between SDO and GONG were manually corrected by comparing the centroids of sunspots visible in HMI continuum images and GONG images simultaneously. IRIS shows good alignment with AIA, with minor misalignments corrected by comparing bright points in the IRIS slit-jaw images with AIA 304 Å images. Lastly, THEMIS was aligned with GONG and IRIS by comparing filament contours. The SOT/SP longitudinal magnetic field magnetograms were manually aligned with HMI data by comparing the magnetic polarities observed in both datasets. We also use the HMI vector magnetograms for the 3D reconstruction of filament magnetic structures.

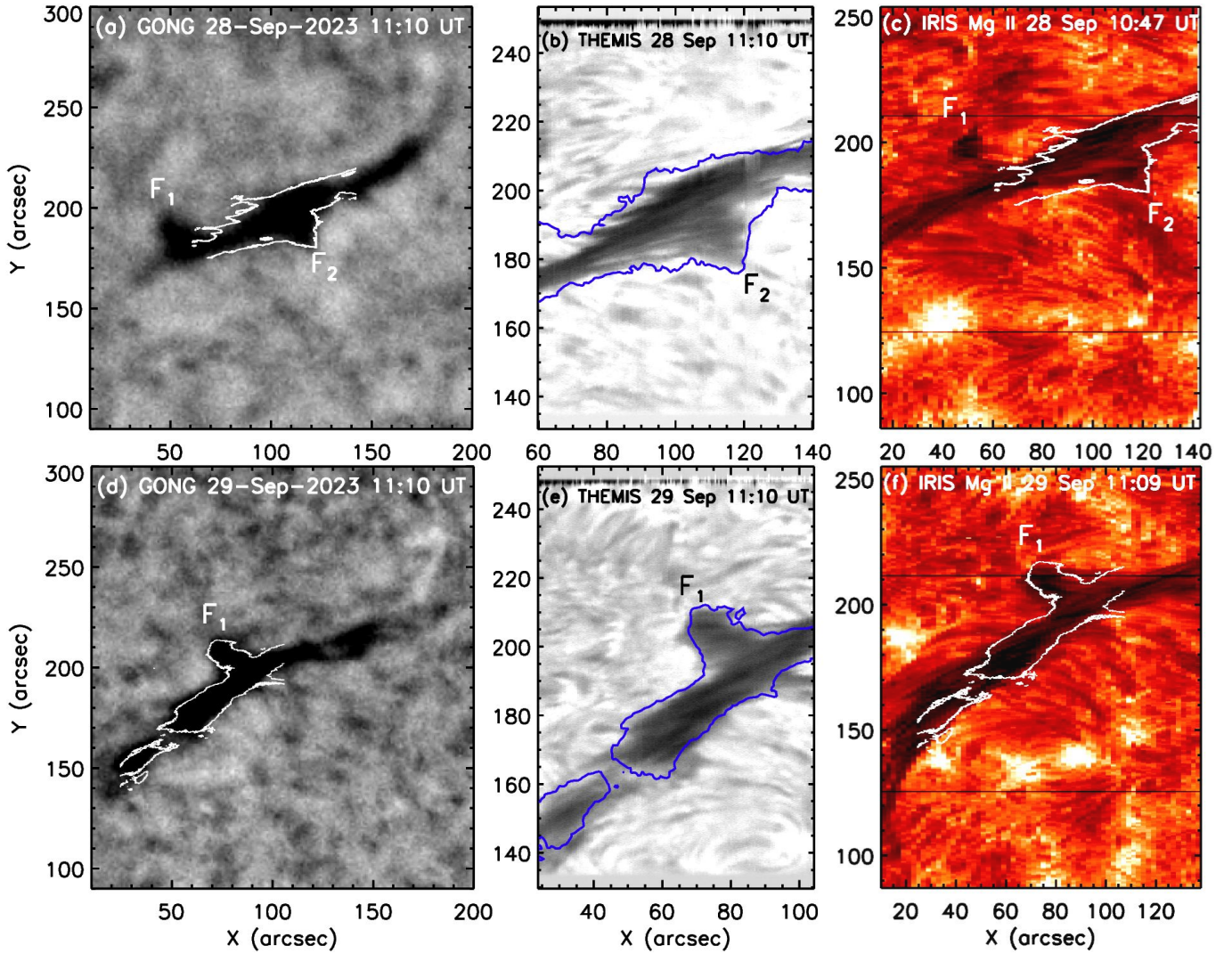


Figure 4. Zoomed view of the filament observed by GONG (panel a) in H α , and the slit-reconstructed images from the spectra in H α line center observed by THEMIS (panel b), and in Mg II k line center (2796.4 Å) by IRIS (panel c), for September 28 and in d, e, f for September 29. The contours (blue) of the filament observed in GONG are overlaid on the THEMIS image, and the filament contours from THEMIS are overlaid in white over GONG and IRIS images to show the THEMIS FOV, which is focused on F₂ on September 28 and on F₁ on September 29. These images are aligned with the X coordinate at 11:00 UT on September 29. Fine structures in the filament are visible in THEMIS and IRIS maps.

2.2. Morphology

A filament near the central meridian was the target of the THEMIS campaign for two days on September 28 (N17, E07) and September 29, 2023 (N17, W06). The filament extends in the middle of the added black squares in Figure 1. A small, separated filament portion is also present in the north-west (still within the squares).

Figure 2 presents snapshots of the region, one for each day observed by GONG (panels a, d). The filament, located around the panel centers, is mostly oriented east-west at an angle of about 10°, with respect to the solar equator on September 28. Two feet are present on September 28 (F₁ and F₂), and only one (F₁) is present on September 29. On the second day, the eastern part of the filament extends and bends southward up to F₃. Panels b and e of Figure 2 show snapshots of the HMI movie for these two days with levels ± 100 G. The filament lies along the PIL between positive polarity in the north and negative polarity in the south, spanning a length of ≈ 180 -380 arcsec. It is a region of a network with identifiable supergranules.

The campaign targeted the southern/main part of the filament, represented by the white contour in Figure 2 panels (b, c, e, f). The presence of feet is correlated with the presence of parasitic polarities visible in the SOT/SP

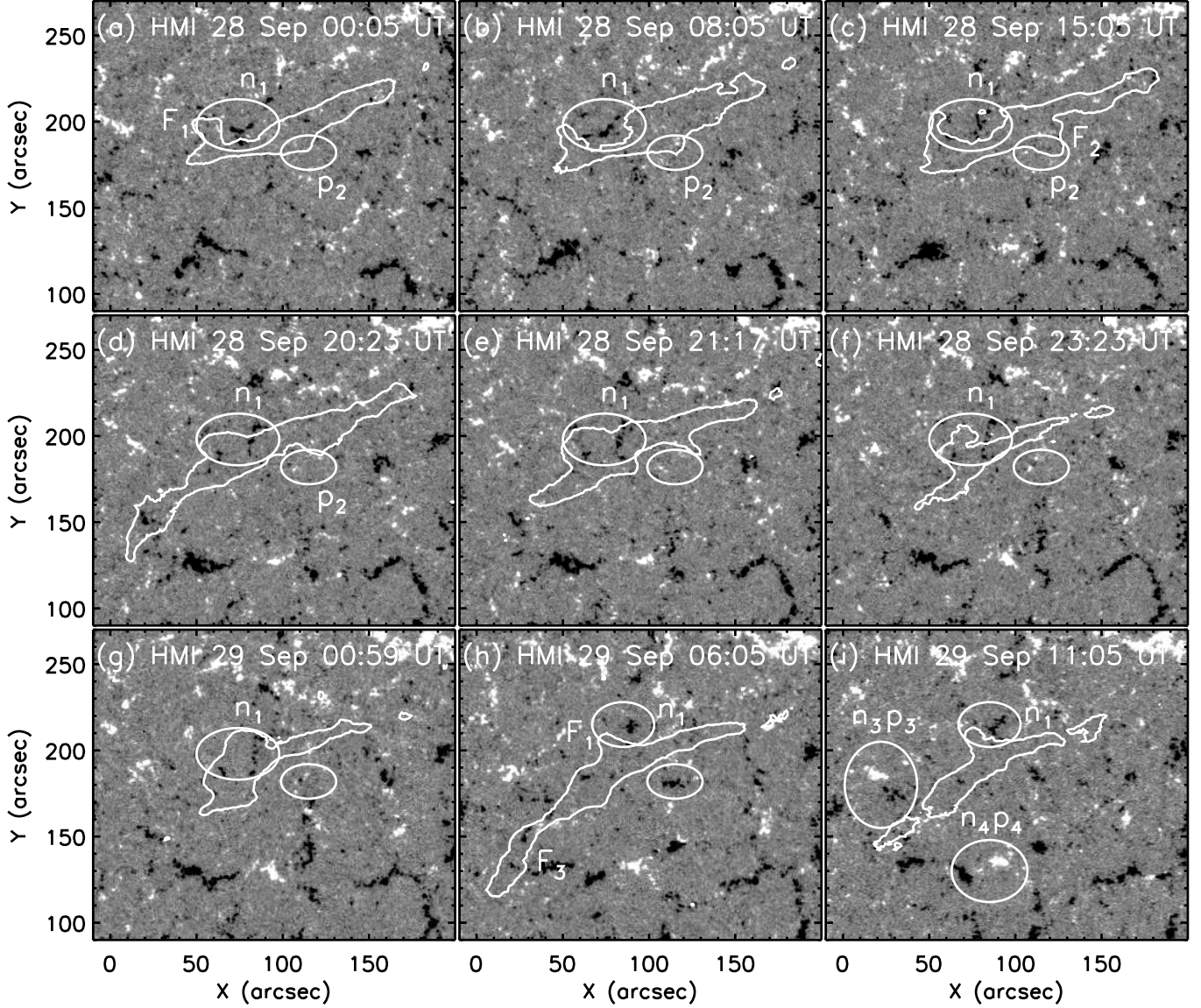


Figure 5. Filament contours and magnetic field evolution. The magnetograms are displayed with magnetic field levels of ± 50 G for the positive and negative polarities, respectively. The white contours in each panel are the filament contours observed in GONG corresponding to the HMI magnetogram time. Panel a correspond to the initial phase of the formation of foot F_2 located near the very small positive polarity p_2 . Panel b corresponds to the 1st maximum of polarity p_2 at around 08 UT, shown by the left red arrow in Figure 6 b. Panel c shows a slight decrease in p_2 . Panel d is when F_2 has disappeared. Panel e is when F_2 reappears around 21 UT. Panel f corresponds to the 2nd maximum of p_2 . We also observe a small negative polarity within p_2 and the disappearance of F_2 . In panel g, the negative polarity within p_2 is stronger, and none of the filament feet are clearly identifiable. In panel h, a strong negative polarity has emerged at the location of p_2 , which corresponds to the maximum of the blue curve in Figure 6 b at around 06 UT on September 29. In panels h and i, we observe two bipoles $n_3 p_3$ and $n_4 p_4$ (ellipses in panel i) and the extension of the filament up to F_3 . An animation of this figure is attached. The animation starts at 23:59 UT on 27 September and ends at 23:53 UT on 29 September. The animation's real-time duration is 1 min 20 s. (An animation of this figure is available in the online article.)

magnetograms with levels ± 100 G (Figure 2 panels c and f). Foot F_1 is related to the parasitic polarity n_1 , and foot F_2 is related to the positive polarity p_2 . The filament extends up to F_3 between the two new bipoles ($n_3 p_3$, $n_4 p_4$) on September 29 (panel f).

Figure 3 compares the filament images observed on September 28 and 29 in AIA 304 Å, AIA 193 Å, and the corresponding HMI magnetograms. In the 304 Å images, we identify a filament channel up to F_1 at 12:18 UT on

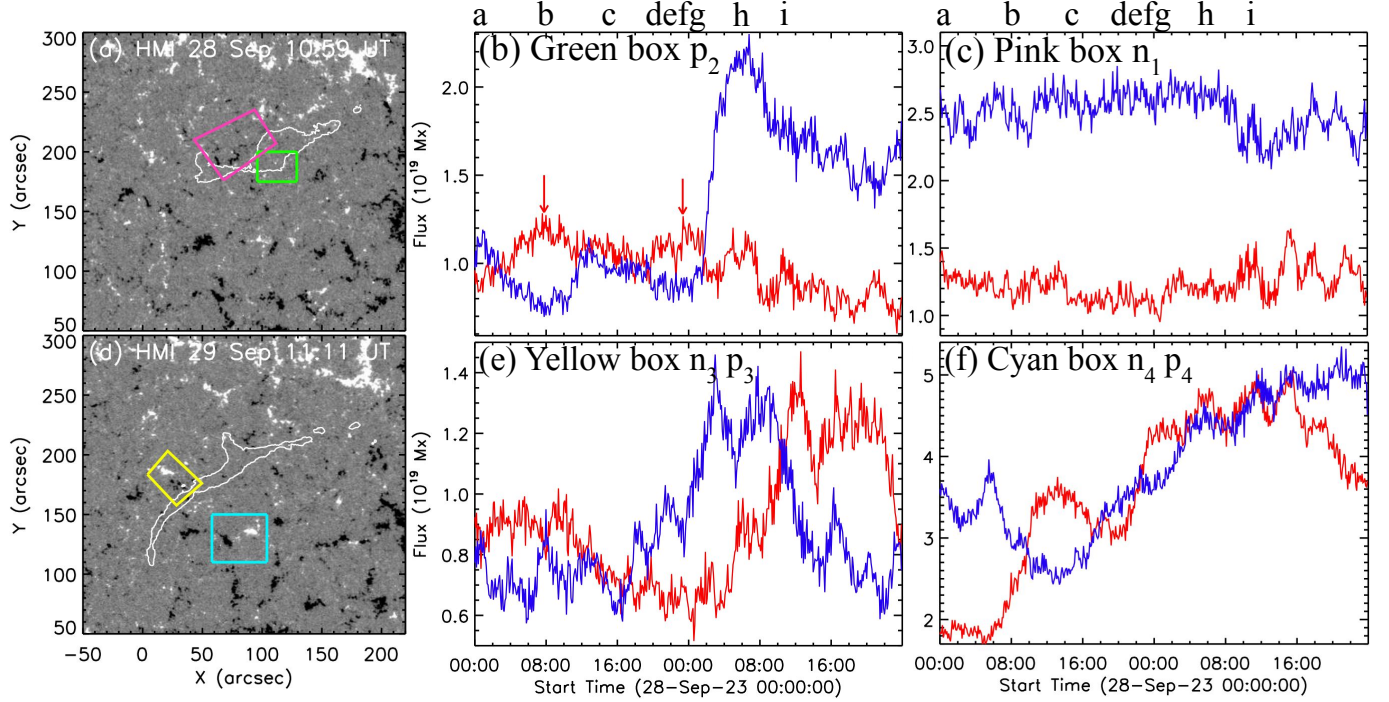


Figure 6. HMI line-of-sight magnetograms (with levels ± 70 G) of the filament channel for September 28 and 29 in panels a and d, respectively. The filament contours observed in GONG for the corresponding times are overlaid in panels a and d. The temporal evolution of the magnetic flux is shown in panels b (green box), c (pink box), e (yellow box), and f (cyan box), with the boxes in panels a and d. The green box is located over polarity p_2 and the panel labels of Figure 5 are added on the panel top. The red and blue curves correspond to positive and negative polarity, respectively. The red arrows in panel b correspond to the maximum of the positive parasitic polarity p_2 . An animation of panels a and d is available, starting on 27 September at 23:59 UT and ending at 23:53 UT on 29 September. The animation's real-time duration is 1 min 20 s. (An animation of this figure is available in the online article.)

September 28 (Figure 3 panel a). On September 29, the filament channel extends to the south and corresponds to the end F_3 (Figure 3 panel d). On both sides of F_3 there are two bright, tiny regions that correspond to the dipoles n_3 , p_3 , and n_4 , p_4 (Figure 3 panel f). These bright points are also well visible in 193 Å (Figure 3 panel e). We will discuss their role in Section 2.4.

In 193 Å the optical thickness of the cool material absorption is similar to the optical thickness in H α (U. Anzer & P. Heinzel 2005). Therefore, the denser part of the filament appears as a strong dark line and corresponds to the region with the largest optical thickness in the filament in H α (panels b, e). This line is overlaid on the HMI magnetograms (blue curve in all panels). We observe that the northwestern part of the filament exhibits a similar structure on both days, though it is slightly more curved on September 29.

2.3. Evolution of feet F_1 and F_2 versus the evolution of the magnetic field

The coordinated observations of THEMIS and IRIS were focused on September 28 on foot F_2 and on September 29 on foot F_1 . Figure 4 shows the relationship of the observations of feet F_1 and F_2 with THEMIS and IRIS for the two days. The high spatial resolution of the instruments allows us to see the fine strands along the filament and in the feet. The adjacent threads have widths of the order of one arcsec. The fine structure makes a small angle with respect to the main axis (about 20 degrees). The foot F_1 has been well studied in H α and Mg II lines in a previous paper, which showed strong counterstreaming in the adjacent threads, with velocities of up to 20 km s $^{-1}$ (G. Karki et al. 2025).

The evolution of the feet F_1 and F_2 is presented in the GONG movie and with white contours in Figure 5. The filament remains highly dynamic on both days. Moreover, the filament changes its shape drastically between 15 UT (1st day, panel c) and 06 UT (2nd day, panel h). On the first day, the foot F_1 is clearly observed at 00 UT and is related to the negative polarity n_1 (panel a). F_1 gradually fades between 15 UT and 20 UT (panels c, d), from its initial position, and reappears slightly north-westward at around 23 UT (panel f). After that, F_1 changes its shape and size continuously, becoming more extended around 06 UT on the next day (panel h), and remains in this state

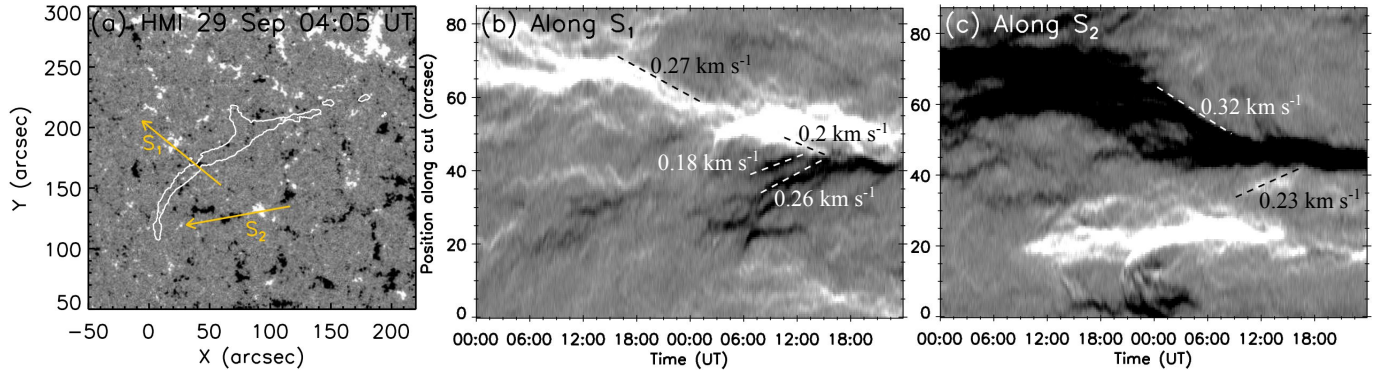


Figure 7. HMI magnetogram (± 50 G) on 29 September 2023 with filament contours in white (panel a). S₁ and S₂ show the slit positions defined to follow the local motions of bipoles n₃ p₃ and n₄ p₄. The slit width is 4.8''. Panels b and c show the time-distance diagrams for slits S₁ and S₂, respectively. Straight lines are defined to follow locally the polarity motions. Their slopes provide the indicated velocities.

throughout the day. Next, the foot F₂ is well-defined between 00:00 UT and 15:00 UT on September 28 (panels a-c), then it becomes diffused and fades out. The foot F₂ reappears around 21 UT (panel e) and then disappears the next day.

The HMI movie of the two days shows the evolution of the magnetic pattern in the filament region. Figure 6 summarizes the time evolution of the magnetic field flux in boxes containing the parasitic polarities n₁, p₂, n₃ and p₃, n₄ and p₄ related to F₁, F₂, F₃, respectively. For the flux computation within the boxes, all HMI magnetograms are aligned to a common reference time (September 29, 2023, at 11:00:00 UT) to compensate for solar rotation. The boxes used to compute the magnetic flux are defined on the aligned data to properly track the magnetic polarities. The panel labels of Figure 5 have been added to the top of the panels of Figure 6 to link the magnetic flux evolution to the magnetogram evolution.

The polarity n₁ (pink box in panel a) is present on both days and is moving slightly to the east. This is why we adopt an elongated box shape to follow n₁. We have noted previously that F₁ is also progressively moving slightly to the east. The magnetic flux measured in the corresponding box containing n₁ shows a nearly constant high negative flux for both days, around 2.6×10^{19} Mx (Figure 6 c). The parallel evolution of n₁ and F₁ further illustrates the model of [G. Aulanier & P. Démoulin \(1998\)](#) and [G. Aulanier et al. \(1999\)](#), which shows that a filament foot is due to the presence of a parasitic polarity and evolves with it.

The formation of F₂ is related to the increase in the magnetic flux of p₂ with a maximum flux of 1.3×10^{19} Mx (see the left red arrow close to the red line in Figure 6 panel b), while the negative flux (blue line) is decreasing to 0.7×10^{19} Mx between 00:00-08:00 UT on September 28. Later on, F₂ reappears on September 28 at around 21 UT (Figure 5, panel e), which can be explained by the increase in the positive polarity to 1.2×10^{19} Mx at around 20 UT (right red arrow in Figure 6 panel b). The disappearance of F₂ on September 29 is associated with a decrease in the positive flux, while the negative flux remains steadily increasing. These related evolutions provide additional evidence for the link between filament foot and parasitic polarity. Finally, we note the rapid increase of negative magnetic flux (blue line) in Figure 6 panel b after 06:00 UT. This corresponds to the entrance of a negative polarity in the selected green box, and it could also contribute to the disappearance of F₂.

2.4. Extension/elongation of the filament to F₃

The filament extends to F₃ on September 29 (Figure 2 d). The extension F₃ and its filament channel are expected to be related to the evolution of the photospheric magnetic field. Then, our analysis first focuses on the appearance of two bipoles on both sides of the filament channel in HMI maps (Figure 6 d, yellow and cyan boxes). The HMI movie allows us to follow their time evolution.

Figure 6 (panel d) shows the bipole n₃ p₃ (yellow box) and its magnetic flux evolution (panel e). The proximity of the two polarities gives the impression of an emerging flux. Moreover, it is associated with an EUV bright point (Figure 3, panels d, e). However, this bipole does not correspond to an emerging bipole but to the transport of a negative magnetic polarity that emerged earlier within the filament channel. In the movie, we observe that small polarities form within supergranules in the channel. Next, they rapidly move to the supergranule borders, where small-scale

cancellations change their shapes and fluxes. Then, the tiny negative polarities forming n_3 rapidly cross the PIL, gather near p_3 , which is also moving quickly, and enter the box around 08 UT on September 29. To better follow this evolution, we perform a time distance plot (Figure 7 b). Finally, the polarity n_3 progressively cancels p_3 by the end of September 29, and we note that, already on September 28 before midnight, there is a slight cancellation. In a very similar study of filament formation (B. Schmieder et al. 2014), the granules were used to compute the displacement of the parasitic polarities. Supergranules were identified, and the parasitic polarities of the feet were found to be located at the borders of supergranules. The same process was also noted in H. T. Li et al. (2022).

On the other side of the filament, another bright point corresponds to the magnetic polarities n_4 p_4 (Figure 6 d, f). At first glance, it appears to correspond to the emergence of a bipole; however, it is also due to the transport of negative polarity toward positive polarity. The bipole is formed by the convergence of n_4 towards p_4 . The positive polarity flux p_4 is mainly increasing on September 28, while the negative polarity is moving to the west at a velocity $\approx 0.3 \text{ km s}^{-1}$ on September 29 (Figure 7 c). Both polarities enter the cyan box (Figure 6 d) and are approaching each other, but the positive and negative fluxes only weakly cancel (Figure 7 c).

In the AIA 193 Å movie, attached to Figure 3, we note the extension evolution of the coronal arcades above the bipoles n_3 p_3 and n_4 p_4 , which is expected to be linked to the observed filament located in between. Figure 8 c displays a zoom of the possible link between the two bipoles, where the elongated and corner-like shape of the plasma emission indicates that magnetic null points are plausibly present. There is even the presence of a loop-like emission in between the two bipolar regions (outlined by a white dashed line). We interpret it as the separator linking the two null points. A separator is the intersection of two separatrices which are locally the fan planes of the null points. The trace of these separatrices, separating plasma regions with different magnetic connectivities, is outlined by an abrupt change of AIA 193 emission. These separatrix traces are outlined by white dashed lines in Figure 8 c. Finally, the plasma trace of the separator partially disappears before the filament reforms, suggesting a plausible local magnetic-field reconfiguration if the evolution is not purely thermal. Finally, the emission evolution of the coronal arcades above the bipoles n_3 p_3 and n_4 p_4 , shown in Figure 8 b, d, will be described within the next subsection in relationship with the filament oscillations.

Next, we study the magnetic field present in the filament channel. The HMI movie presents the evolution of magnetic flux in the filament channel (see the attached movie). Tiny emerging polarities develop inside supergranules and move across the PIL. The two former studied bipoles are examples, but there are many other tiny bipoles with very low magnetic flux. It is difficult to track changes in supergranules, and even more challenging to monitor the emergence of tiny polarities within them. These changes in the movement and cancellation of magnetic flux could help the filament channel extend to F_3 . Similarly, H. T. Li et al. (2022) explains the extension of their studied filament by successively cancelling flux below the filament. This supports the model of A. A. van Ballegooijen & P. C. H. Martens (1989).

2.5. Longitudinal Amplitude Oscillations

We have observed oscillations in the filament along a slit parallel to the main filament axis. Therefore, the observed oscillations are almost longitudinal in nature. These longitudinal oscillations along the filament spine are observed over two days using GONG data. The data for both days have been aligned to a common reference time, as described in Section 2.1. To analyze the longitudinal amplitude oscillations along the filament, we employ the time-distance method using a curved slice S , oriented from southeast to northwest, to trace the plasma motions along the filament spine (Figure 9 a). Figure 9 b presents the time-distance plot for the filament observed from September 28 at 10:00 UT until September 29 at 23:59 UT, during which the extension F_3 becomes visible. Figure 9 c is a zoom during the time period with more/larger oscillations. The gaps present in the data are indicated by the black regions in the time-distance plot. The filament structure undergoes significant changes during this time period (see the accompanying GONG movie).

Longitudinal oscillations are detected at both ends of the filament on September 29, where the contrast with the surroundings is higher. In the center of the filament, the oscillations seem to be mixed because of a larger number of fibrils. Moreover, the oscillations may not be exactly along the main axis of the filament, but rather along the fine structures of the filament, which make an angle of approximately 20 degrees (see section 2.3). On September 29, a few oscillatory cycles were detected near F_3 between 08:00 and 12:00 UT (Figure 9 b). These oscillations are preceded by two tentative extensions around 21:00 UT on September 28 and around 03:00 UT on September 29. The oscillation period is approximately 70 min. It is a common period for filament longitudinal oscillations (M. Luna et al.

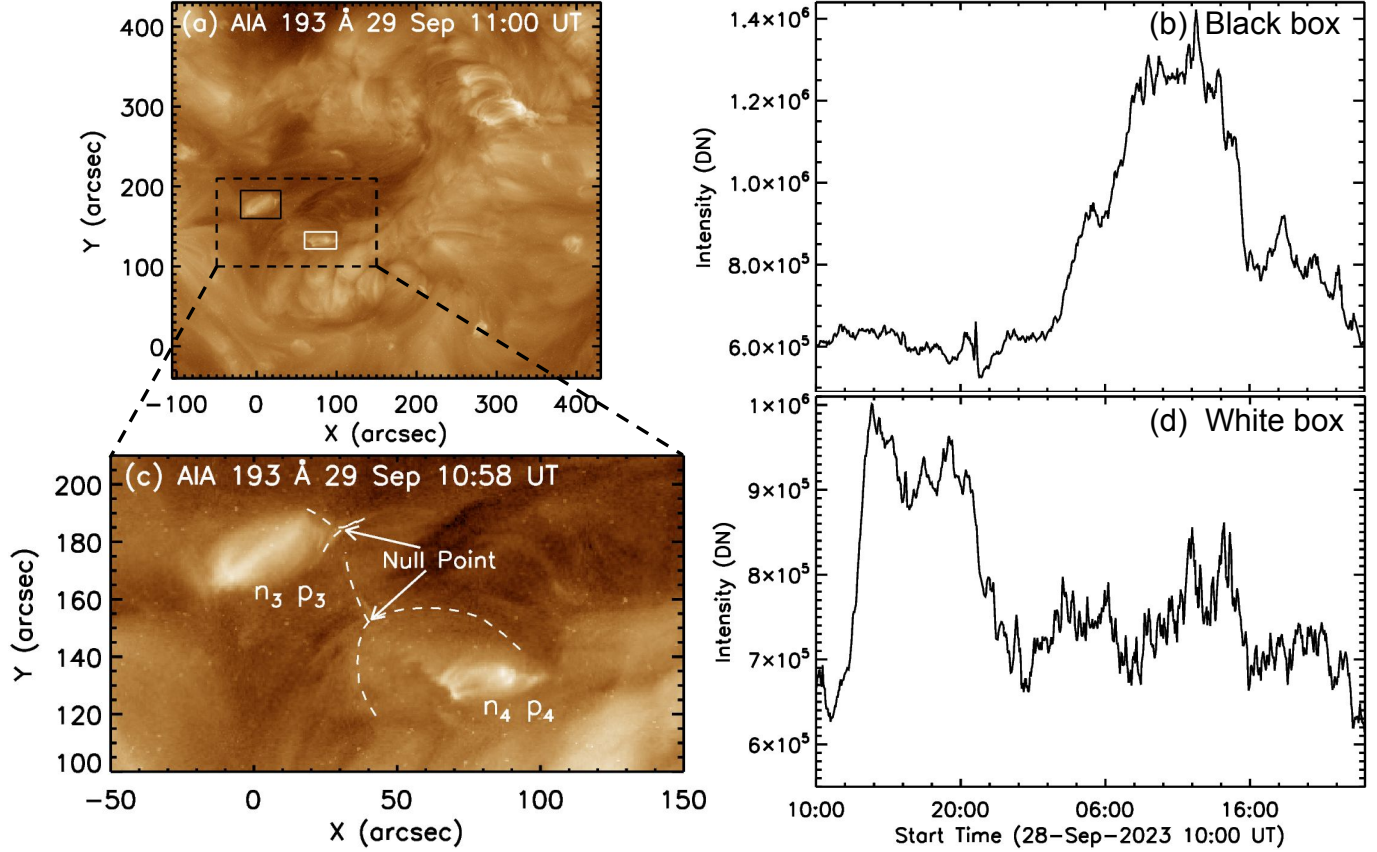


Figure 8. Panel (a) shows the filament observed in AIA 193 Å. The black dashed box shows the FOV of panel (c). The black and white small solid box shows the regions in which the intensity is plotted with time (panels (b) and (d)). Panel (c) shows brightenings observed in AIA 193 Å corresponding to the two bipoles $n_3 p_3$ and $n_4 p_4$. The white arrows show the possible magnetic null points above the two bipoles. The loop-like connection between the nulls, plausibly a plasma trace of the separator linking them, is outlined in a dashed line. Other dashed lines indicate intensity limits that plausibly mark separatrices. Panels (b) and (d) represent the intensity variation within the black and white boxes shown in panel (a), respectively.

2018, 2022). Moreover, several threads along the filament spine also display oscillatory behavior in the time–distance diagrams on both days.

The longitudinal amplitude oscillations along F_3 reflect its dynamical evolution. On September 29, after 12 UT, parts of the extension F_3 are relatively stable. The filament magnetic structure with a long FR may have tentatively existed previously (e.g., around 20:23 UT on September 28). Photospheric motions lead to emerging magnetic flux, which then cancels, and heating as a consequence of reconnection. This process supplies energy into the overlying magnetic configuration and the plasma embedded within it. In Figure 8 b, the intensity curve over $n_3 p_3$ shows an enhancement at approximately the time of the longitudinal oscillations in F_3 between 08:00 UT and 12:00 UT. The evaporation of the hot plasma during reconnection could trigger longitudinal oscillations, pushing the cold plasma along the magnetic field lines. This initiates a pendulum mode of the cool plasma that fills a larger portion of the magnetic dips (M. Luna et al. 2012, 2018; Q. M. Zhang et al. 2017). Such a relationship is not clear with the earlier brightness evolution over $n_4 p_4$ (Figure 8 d) as F_3 was not well formed at that time.

3. NUMERICAL CONSTRUCTION OF 3D MAGNETIC FIELDS OF FILAMENTS

3.1. Numerical setup

To investigate the 3D magnetic structures of solar filaments, we reconstruct their 3D magnetic fields with the magneto-frictional method, in which the initial magnetic fields are provided by the potential field extrapolation and the Biot-Savart laws regularized in FR model (V. S. Titov et al. 2018). The resulting magnetic field is magneto-

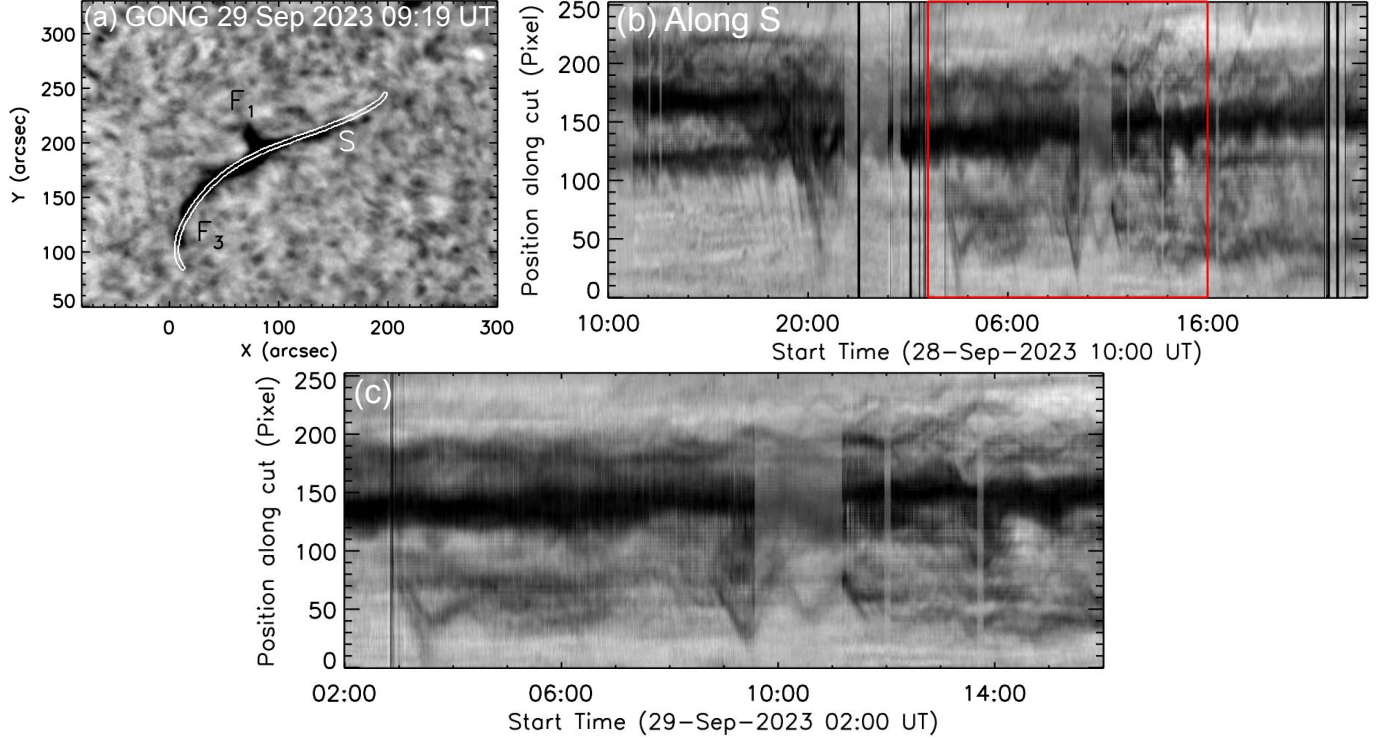


Figure 9. Panel (a) presents the filament observed by GONG on September 29. The white curve S is the slit used to detect the filament motions. The slit is oriented from south-east to north-west. F_1 is a footpoint of the filament, and F_3 is the extension to the south. The slit width is 2 pixels. Panel (b) shows the time-distance diagram along the slit S. The time-distance diagram enclosed within the red box (from 02:00 to 16:00 UT on September 29) is shown in panel c.

frictional relaxed to a non-linear-force-free-field (NLFFF) extrapolation based on Y. Guo et al. (2016b,a). This is achieved in the MPI-AMRVAC framework (C. Xia et al. 2018; Y. Guo et al. 2016b,a, 2019; J. H. Guo et al. 2021a).

The implementation process is as follows. First, we correct for projection effects and remove the Lorentz force and torque using an optimisation technique to conform to the force-free assumption (T. Wiegelmans & T. Neukirch 2006). Hereafter, we extrapolate the potential magnetic fields using the Green's function based on the vertical B_z component of the preprocessed vector magnetogram. Next, we insert a FR with regularised Biot-Savart laws, in which the parameters are constrained by the observed filament shape, as described in (Y. Guo et al. 2019) and J. H. Guo et al. (2021a). The parabolic profile for the current density is adopted in this model, leading to a FR with a strongly twisted core and a weakly twisted outer shell (J. H. Guo et al. 2021a).

The FR is mainly controlled by four parameters: the FR path (C), minor radius (a), toroidal flux (F), and electric current (I). Among them, the first two parameters are approximated as the filament path and width, respectively. The toroidal flux is estimated as the average unsigned flux of two flux-rope footpoints, and the electric current is calculated by the equilibrium condition (V. S. Titov et al. 2018). Then, the combined potential and FR fields are relaxed to a force-free state using the magneto-frictional method. The computational domain of the model on September 28 and 29 is $[x_{min}, x_{max}] \times [y_{min}, y_{max}] \times [z_{min}, z_{max}] = [-180, 180] \times [-180, 180] \times [1, 307] \text{ Mm}^3$ and $[x_{min}, x_{max}] \times [y_{min}, y_{max}] \times [z_{min}, z_{max}] = [-211, 211] \times [-160, 160] \times [1, 322] \text{ Mm}^3$, respectively.

3.2. Results analysis

Figures 10 and 11 display the 3D magnetic structures of the filament on September 28 and 29, along with comparisons to GONG H α observations, respectively. Both observations and NLFFF extrapolation show that the filament consists of two separate parts (yellow and green field lines). In the previous section, only the southern part was analyzed. Here, we consider both sections, north and south.

On September 28, the southern part consists of a twisted FR with deep magnetic dips, while the northern part corresponds to a sheared arcade with shallow dips (Figure 10). According to J. H. Guo et al. (2022) and J. H. Guo et al. (2021b), stationary filament threads are more prone to remain in deep dips with FRs, whereas dynamic

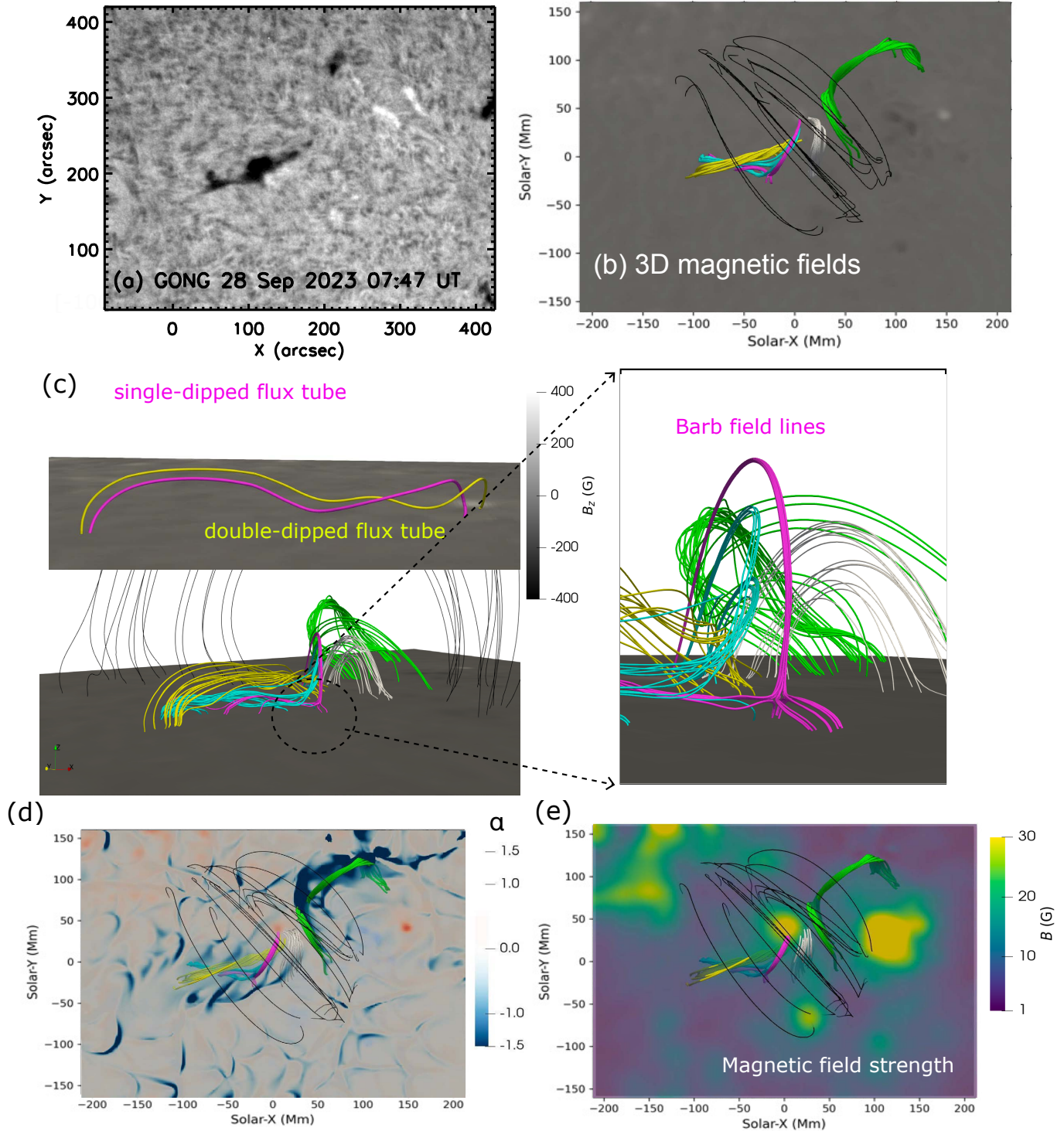


Figure 10. Filament observation on September 28 by GONG in helioprojective coordinates (a) and 3D reconstruction of the coronal magnetic structures in the local coordinate system after projection correction (b–e). The yellow and green field lines show the southern and northern parts of the filament spines, respectively. The cyan and magenta lines represent the field lines hosting filament feet F_1 and F_2 in positive and negative main polarities, respectively. The zoomed views in panel (c) show field lines associated with the feet as viewed from the side. Panels (d) and (e) display, at $z = 20$ Mm, the distribution of twist density ($J \cdot B/B^2$) and magnetic-field strength, respectively, with overlaid the magnetic field lines in yellow, green, magenta and cyan. The green field lines in the extrapolation correspond to the filament material in the northern part, where continuously distributed magnetic dips are lacking and thus cannot support a long, coherent filament as in the southern part.

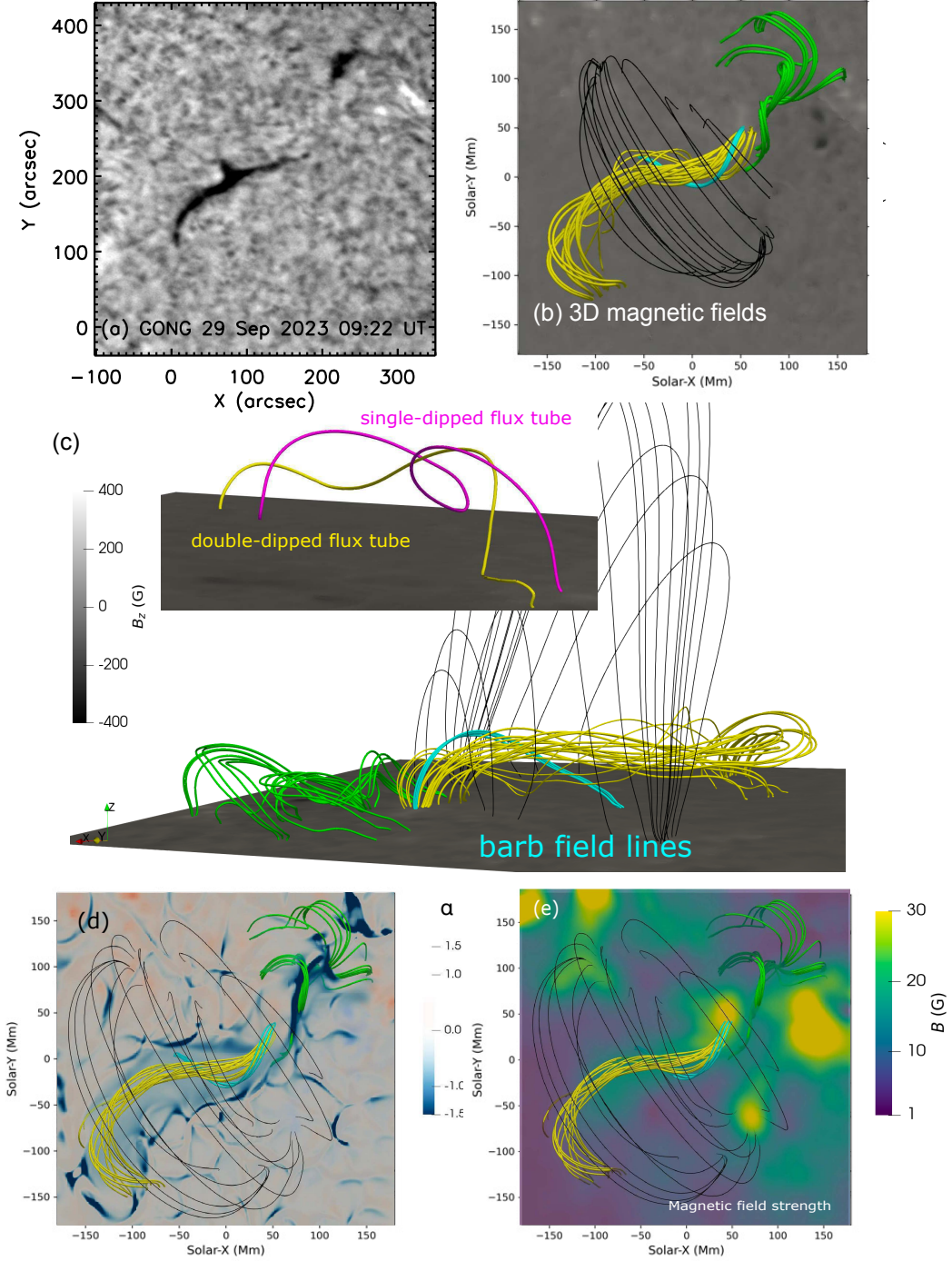


Figure 11. The same as Figure 10 but for the filament on September 29.

threads formed due to the thermal non-equilibrium cycle favor weakly twisted FRs and sheared arcades. The magnetic structure on September 29 is still composed of two parts, while the southern FR (yellow lines) is more extended (Figure 11). Some field lines of the southern FR are nearly joining the northern positive parasitic polarities, while those in the south connect to the southern negative parasitic polarities. Our numerical model can explain the following observational phenomena.

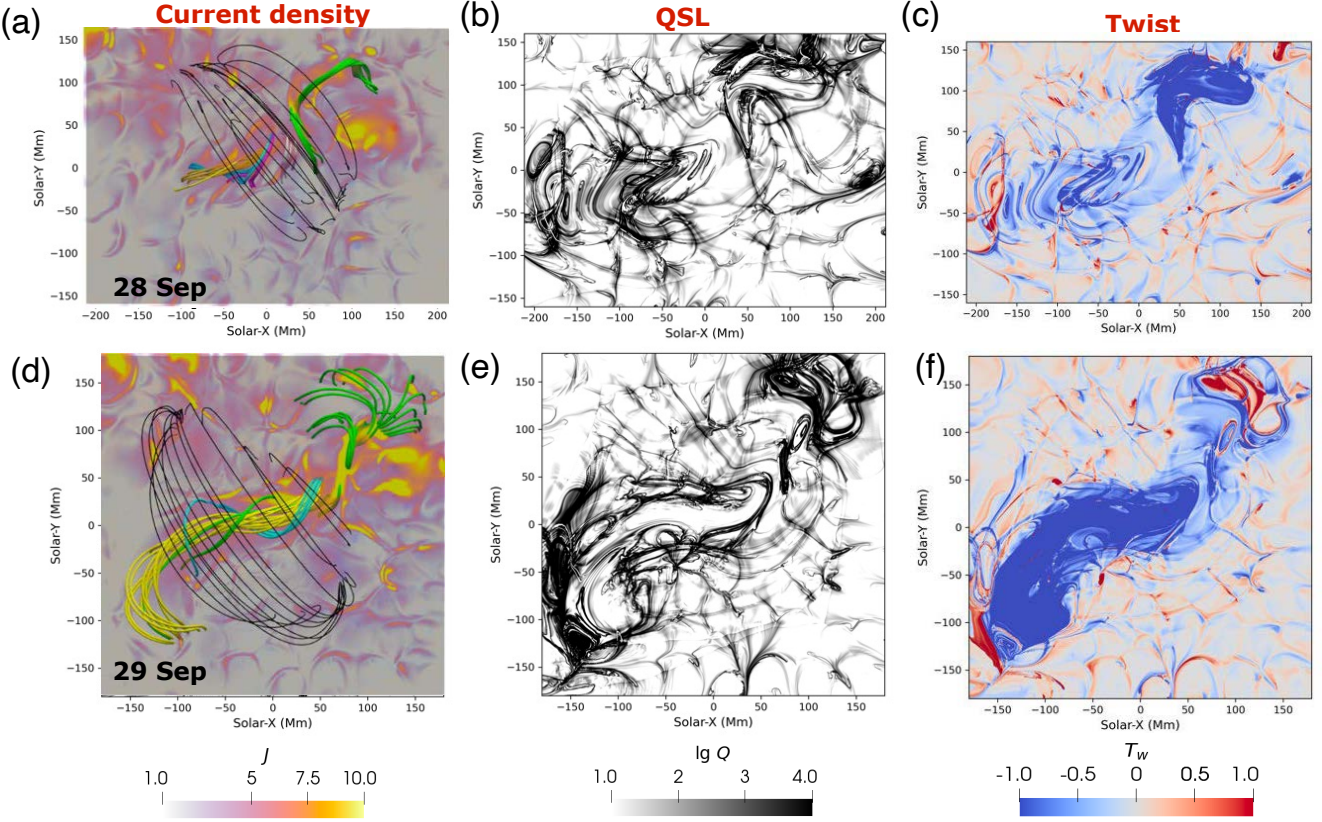


Figure 12. Current density, quasi-separatrix layers (QSL), twist maps computed for the filament on September 28 (panels a, b, c) and for September 29 (panels d, e, f). The unit of the current density is 10^{-2} A m^{-2} .

First, the magnetic structure of the studied filament is a FR composed of two separate parts, deviating from a coherent structure, which can explain the two portions of the filament in observations (as shown in Figures 10 a and 11 a). The magnetic configuration in the southern segment corresponds to an FR, while that in the north is a sheared arcade, producing a greater number of magnetic dips that can host more filament plasma.

Second, regarding the formation mechanism of filament feet, it is found that the foot F_2 is due to the positive parasitic magnetic polarity p_2 embedded in negative polarities (magenta lines in Figure 10). The zoomed image of Figure 10 c shows, with magenta field lines, the fan-spine structure associated with a magnetic null point. It is due to the existence of p_2 nearby. Next, the foot F_1 corresponds to twisted field lines (cyan lines) located below the spine field lines (yellow lines). For the filament on September 29, the foot F_2 disappears with the vanishing of the parasitic polarity p_2 . However, the foot F_1 becomes more developed with the growth of the FR.

Third, the comparison between the 3D magnetic structures on September 28 and 29 reveals the filament extension F_3 with more extended south-eastward twisted yellow field lines in Figure 11 than in Figure 10. This explains the increase in the filament extension observed by GONG (panels (a) of the same figures). F_3 is located within the yellow field lines (Figure 11). The modeled FR is also consistent with the numerous filament threads along the filament spine detected in high-resolution observations (Figure 4).

Fourth, in Figures 10 d and 11 d, the twist density is shown at $z = 20 \text{ Mm}$. The twist density is defined as $\alpha = \vec{J} \cdot \vec{B}/B^2$, which indicates how much the field lines are non-potential. We note a significant change between the two days with the formation of a large channel with low α values around the field lines of the FR (yellow lines). This channel is bordered by intense α values distributed along linear structures, especially on September 29.

Finally, in Figure 12 we present the current density, the quasi-separatrix layers (QSLs) and the twist number for the two days. Quasi-separatrix layers (QSLs) represent regions where magnetic connectivity changes rapidly (E. R. Priest & P. Démoulin 1995; P. Demoulin et al. 1996) and are often used to delineate the boundaries of flux ropes. The twist number is the number of turns along field lines (so a curvilinear integration of α). This is a nondimensional parameter,

and, in particular, it is independent of B magnitude. The twist is weak on September 28 (except in the northern region), then strengthens and extends on September 29. This is traced indirectly by the filament extending southward. Next, at $z = 20$ Mm, most small-scale connectivities have been filtered out, allowing us to observe the large-scale topology with QSLs. They separate the twisted/sheared core of the filament B configuration from the surrounding, more potential arcade (where flux cancellation has not yet been active because it is too far from the PIL). The current density maps show a current layer separating the core from the surroundings, as QSLs do. So on both days, both twist and QSL at $z = 20$ Mm are consistent. Such current concentrations on QSLs, derived from magnetic extrapolation, were previously reported (Y. Guo et al. 2013). With QSLs present, such current layers are expected to form during MHD evolution; here, however, this is inferred from two magnetic extrapolations. This is a confirmation that the extrapolations are capturing well the key aspects of the magnetic configuration evolution. In summary, with these maps for the two days, we can clearly characterize the buildup of the FR between 28 and 29 September with the twist maps, and the separation of the FR from the surrounding more potential fields with the current density and the QSLs.

4. CONCLUSION

Coordinated observations were obtained for two days during a THEMIS campaign in September 2023, involving the Hinode/SOT and IRIS spacecraft. The quiescent filament was also observed by GONG, exhibiting high dynamics during its elongated formation. In addition, THEMIS observations of the filament show multiple strands in its spine and feet. The long-term study shows large-amplitude oscillations in the filament’s extension. The evolution of the photospheric magnetic field is well observed with the HINODE/SOT-SP and HMI instruments. Magnetic polarities emerge, then some of them cross the PIL, inducing magnetic cancellation, a key ingredient for FR formation.

Magnetic extrapolations are obtained by inserting an FR into a potential field; then, a magneto-frictional method is applied. The deduced magnetic configurations include two separate regions having magnetic dips. They are located where the two filament parts are observed (along the same PIL). The FR extends in length between the two days, as the filament does in the observations. This changing shape is due to the emergence of magnetic flux, which then cancels magnetic polarities.

The observations and magnetic extrapolations provide key insights into the formation and extension of the filament:

- The formation mechanism of filament feet is consistent with the dip model (G. Aulanier & P. Démoulin 1998). Dips are due to field lines being “attracted” by magnetic parasitic polarities with opposite signs to the background. The feet evolve with the parasitic polarities.
- The filament extension is formed progressively by canceling flux along the PIL. This progressively transforms the sheared magnetic field into an FR.
- Large amplitude oscillations are observed to develop in a fraction of time during the two days. In the filament channel, cancellation and polarity motions impose an evolution on the magnetic polarities. Therefore, the magnetic dips change shape and location, which forces the dense plasma to evolve. Moreover, heating due to magnetic reconnection of a dipole at the channel boundary is plausibly an energy source for the oscillations. The cold plasma is pushed by the hot plasma, initiating the oscillations. Finally, similar periods of around 70 min for the longitudinal oscillations are observed across different dips. This is in agreement with theory (Y.-H. Zhou et al. 2017).
- The two magnetic dipoles, formed by converging flows at the border of the filament channel, organize the magnetic field lines in the extension of the filament, which develops on the second day.
- We analyze the changes in the magnetic configuration between the two days using 3D MHD reconstruction with two magnetograms. On the 28th of September, the FR begins to form, and the next day it is more extended, in agreement with filament observations. On the 29th of September, the FR is located in a channel bordered by QSLs with high electric currents. They are separating the FR from the nearly surrounding potential field.
- The magnetic extrapolation reveals double-dipped flux tubes, supporting the scenario of magnetically connected threads, as shown in Figures 10 c and 11 c. The second dip corresponds to the extension of the filament in F₃.

The presence of multiple threads along one flux tube introduces new physics. For example, the longitudinal oscillations of the threads are no longer independent, and there is thread-to-thread interaction, which significantly changes the

damping time of the oscillations, sometimes leading to decayless oscillations (Y.-H. Zhou et al. 2017). The signatures of such thread-thread interactions were observed previously (Q. M. Zhang et al. 2017).

In conclusion, these observations and the 3D MHD modeling confirm the importance of the photospheric magnetic field within the filament channel. The magnetic field spatial distribution and temporal evolution structures the magnetic configuration of the filament, and in particular the FR. On September 28 the filament is formed by a split flux tube. One part of the flux tube is rooted in the photosphere aside an observed interruption in the filament. Then, the combination of high resolution observations and numerical modeling is an efficient way to understand the physics present behind the evolution of filaments. The dense and cold plasma caught in the magnetic configuration provides important constraints for the modeling the magnetic configuration evolution. Parasitic polarities, associated with filament feet, result in secondary dips above the related local inversion line. These dips belong to long field lines that pass below the flux tube. Many of these field lines are not rooted near the related foot.

ACKNOWLEDGMENTS

The authors thank the referee for constructive comments and suggestions, which significantly improved the manuscript. This work is based on ground-based observations obtained by the THEMIS telescope in Tenerife in the Canary Islands, operated by Bernard Gelly, Richard Douet, and Didier Laforgue[†] during a multi-wavelength campaign with IRIS (IHOP444 - PIs Nicolas Labrosse and Brigitte Schmieder - coordinated with Hinode by Sarah Matthews). Hinode is a Japanese mission developed and launched by ISAS/JAXA, with NAOJ as a domestic partner and NASA and STFC (UK) as international partners. It is operated by these agencies in co-operation with ESA and NSC (Norway). The H α spectroheliograph was provided by BASS2000.obspm.fr. AIA data are courtesy of NASA/SDO and the AIA, EVE, and HMI science teams. IRIS is a NASA small explorer mission developed and operated by LMSAL, with mission operations executed at NASA Ames Research Center and major contributions to downlink communications funded by ESA and the Norwegian Space Centre. B.S. thanks Rony Keppens and Tom Van Doorsselaere for fruitful discussions on waves and filament fine structures. G.K. acknowledges support from DST INSPIRE. J.H.G. is supported by the fellowship of the China National Postdoctoral Program for Innovative Talents under Grant Number BX20240159. S.P. is funded by the European Union (ERC, Open SESAME, 101141362). Views and opinions expressed are, however, those of the author(s) only and do not necessarily reflect those of the European Union or the European Research Council. Neither the European Union nor the granting authority can be held responsible for them. S.P. is funded by the projects C16/24/010 (C1 project Internal Funds KU Leuven), G0B5823N and G002523N (WEAVE) (FWO-Vlaanderen), and 4000145223 (SIDC Data Exploitation (SIDEX2), ESA Prodex).

AUTHOR CONTRIBUTIONS

G.K. provided the formal analysis of the data and validation. She also edited the manuscript. J.H.G. is responsible for the numerical simulations. B.S. and R.C. supervised the work and partly wrote the manuscript. P.D. edited the manuscript. S.P. revised the manuscript. B.G. was providing the THEMIS observations.

Facilities: GONG, IRIS, Meudon spectroheliograph, SDO (AIA and HMI), Hinode/SOT, and THEMIS.

APPENDIX

A. DESCRIPTION OF INSTRUMENTS

The Solar Dynamics Observatory (SDO; W. D. Pesnell et al. 2012) consists mainly of two instruments: the Atmospheric Imaging Assembly (AIA; J. R. Lemen et al. 2012) and the Helioseismic and Magnetic Imager (HMI; J. Schou et al. 2012). The AIA observes the full Sun in seven extreme ultra-violet (EUV; 94, 131, 171, 193, 211, 304, 335 Å), two ultra-violet (UV; 1600, 1700 Å) and one white light (4500 Å) wavebands, with a pixel size and temporal sampling of 0.6'' and 12 s, respectively. Here, we have mainly used AIA 193 and 304 Å filter data to observe the filament. HMI provides the photospheric magnetic field. It observes the Sun at a wavelength of 6173 Å with a pixel size of 0.5'' and a temporal sampling of 45 s. For the present study, we have used longitudinal magnetograms to analyse the magnetic field of the filament region. We have also used HMI vector magnetograms for 3D numerical reconstruction.

The Interface Region Imaging Spectrograph (IRIS; [B. De Pontieu et al. 2014](#)) provides spectra in three different passbands, 1332 – 1358 Å, 1389 – 1407 Å, and 2783 – 2834 Å, these passbands include several spectral lines such as Mg II h (2803 Å) and Mg II k (2796 Å) formed in the chromosphere, as well as C II (1334/1335 Å) formed in high chromosphere and Si IV (1394/1403 Å) formed in the transition region. IRIS also provides slit jaw images at four different UV wavelengths: Mg II wing (2830 Å), Mg II k (2796 Å), C II (1330 Å), and Si IV (1400 Å). IRIS observed the filament from 10:29:57 UT to 11:22:21 UT, with its FOV centered at $x = -130''$ and $y = 174''$ in coordination with THEMIS on September 28 and from 10:34:17 UT to 11:26:37 UT with the FOV center at $x = 74''$ and $y = 175''$ on September 29. During one observation hour, IRIS acquired 3 rasters with 64 steps, each step, having a size of 2'' covered a FOV of $127'' \times 175''$ in ≈ 20 min, with raster cadence of 1048 s and step cadence of 16.4 s. The slit jaw images are taken in the 2796 Å (Mg II k) wavelength with a cadence of 16 s that covers the FOV of $166'' \times 175''$. The SJIs were obtained only in the Mg II k 2796 Å passband.

The Solar Optical Telescope (SOT; [S. Tsuneta et al. 2008](#)), is one of the three instruments onboard Hinode ([T. Kosugi et al. 2007](#)). The SOT is a 50 cm diffraction-limited telescope equipped with both a filtergram and a spectropolarimeter (SP). The SP instrument acquires the spectra of the two Fe lines at 630.15 and 630.25 nm, along with the nearby continuum. SP can operate in four different modes: normal map, fast map, dynamics, and deep magnetograms. For the current study, we have used SP observations on September 28 at 10:59 UT and on September 29 at 10:35 UT. Both SP observations are operated in fast map mode, with a pixel size of 0.32'' along the slit and 0.30'' transverse to the slit, covering a FOV of $145'' \times 164''$ on September 28 and a FOV of $153'' \times 164''$ on September 29. The spectral scale is ≈ 21.5 mÅ. In this mode, a region of 1.6'' wide is covered in 18 s.

The Global Oscillation Network Group (GONG; [J. W. Harvey et al. 1996](#)) is a network of six identical telescopes located worldwide that provides full-disk images of the Sun in H α wavelength with a pixel size of 2.5'' and a temporal resolution of 1 min. We have used the GONG H α data to analyse the filament.

The Télescope Héliographique pour l'Etude du Magnétisme et des Instabilités Solaires, (THEMIS; [P. Mein & J. Rayrole 1985](#)) built in the 90's and recently renovated with adaptive optics ([B. Schmieder et al. 2025](#)), allows observations in spectropolarimetric mode, a small region of the Sun ($80'' \times 120''$) with a pixel size of 0.06'' along the slit and a spectral dispersion of ≈ 3.067 mÅ per pixel. THEMIS provides spectra from four cameras at different wavelengths. Here, we focus on the H α observations with a passband centred at 6563 Å and 6.3 Å wide. The slit step is either 0.5'' or 1'', with a slit width of 0.5''. Depending on the targets and viewing conditions, the H α exposure time ranges from 0.05 to 0.2 s.

REFERENCES

Amari, T., Canou, A., Aly, J.-J., Delyon, F., & Alauzet, F. 2018, *Nature*, 554, 211, doi: [10.1038/nature24671](https://doi.org/10.1038/nature24671)

Anzer, U., & Heinzel, P. 2005, *ApJ*, 622, 714, doi: [10.1086/427817](https://doi.org/10.1086/427817)

Arregui, I., Oliver, R., & Ballester, J. L. 2018, *Living Reviews in Solar Physics*, 15, 3, doi: [10.1007/s41116-018-0012-6](https://doi.org/10.1007/s41116-018-0012-6)

Asai, A., Ishii, T. T., Isobe, H., et al. 2012, *ApJL*, 745, L18, doi: [10.1088/2041-8205/745/2/L18](https://doi.org/10.1088/2041-8205/745/2/L18)

Aulanier, G., & Démoulin, P. 1998, *A&A*, 329, 1125

Aulanier, G., Démoulin, P., Mein, N., et al. 1999, *A&A*, 342, 867

Aulanier, G., & Schmieder, B. 2002, *A&A*, 386, 1106, doi: [10.1051/0004-6361:20020179](https://doi.org/10.1051/0004-6361:20020179)

Aulanier, G., Srivastava, N., & Martin, S. F. 2000, *ApJ*, 543, 447, doi: [10.1086/317095](https://doi.org/10.1086/317095)

Aulanier, G., Török, T., Démoulin, P., & DeLuca, E. E. 2010, *ApJ*, 708, 314, doi: [10.1088/0004-637X/708/1/314](https://doi.org/10.1088/0004-637X/708/1/314)

Bi, Y., Jiang, Y., Yang, J., et al. 2014, *ApJ*, 790, 100, doi: [10.1088/0004-637X/790/2/100](https://doi.org/10.1088/0004-637X/790/2/100)

Bocchialini, K., Baudin, F., Koutchmy, S., Pouget, G., & Solomon, J. 2011, *A&A*, 533, A96, doi: [10.1051/0004-6361/201016342](https://doi.org/10.1051/0004-6361/201016342)

Chandra, R., Démoulin, P., Devi, P., Joshi, R., & Schmieder, B. 2021, *ApJ*, 922, 227, doi: [10.3847/1538-4357/ac2837](https://doi.org/10.3847/1538-4357/ac2837)

Chandra, R., Pariat, E., Schmieder, B., Mandrini, C. H., & Uddin, W. 2010, *SoPh*, 261, 127, doi: [10.1007/s11207-009-9470-2](https://doi.org/10.1007/s11207-009-9470-2)

Chen, H., Xia, C., Ma, S., et al. 2025, *ApJ*, 994, 27, doi: [10.3847/1538-4357/ae0ad4](https://doi.org/10.3847/1538-4357/ae0ad4)

Chen, P. F., Harra, L. K., & Fang, C. 2014, *ApJ*, 784, 50, doi: [10.1088/0004-637X/784/1/50](https://doi.org/10.1088/0004-637X/784/1/50)

Chen, P.-F., Xu, A.-A., & Ding, M.-D. 2020, *Research in Astronomy and Astrophysics*, 20, 166, doi: [10.1088/1674-4527/20/10/166](https://doi.org/10.1088/1674-4527/20/10/166)

Cheng, X., Zhang, J., Kliem, B., et al. 2020, *ApJ*, 894, 85, doi: [10.3847/1538-4357/ab886a](https://doi.org/10.3847/1538-4357/ab886a)

De Pontieu, B., Title, A. M., Lemen, J. R., et al. 2014, *SoPh*, 289, 2733, doi: [10.1007/s11207-014-0485-y](https://doi.org/10.1007/s11207-014-0485-y)

Demoulin, P., Henoux, J. C., Priest, E. R., & Mandrini, C. H. 1996, *A&A*, 308, 643

Devi, P., Chandra, R., Joshi, R., et al. 2022, *Advances in Space Research*, 70, 1592, doi: [10.1016/j.asr.2022.02.053](https://doi.org/10.1016/j.asr.2022.02.053)

Devi, P., Démoulin, P., Chandra, R., et al. 2021, *A&A*, 647, A85, doi: [10.1051/0004-6361/202040042](https://doi.org/10.1051/0004-6361/202040042)

DeVore, C. R., Antiochos, S. K., & Aulanier, G. 2005, *ApJ*, 629, 1122, doi: [10.1086/431721](https://doi.org/10.1086/431721)

Dudík, J., Aulanier, G., Schmieder, B., Bommier, V., & Roudier, T. 2008, *SoPh*, 248, 29, doi: [10.1007/s11207-008-9155-2](https://doi.org/10.1007/s11207-008-9155-2)

Guo, J. H., Ni, Y. W., Qiu, Y., et al. 2021a, *ApJ*, 917, 81, doi: [10.3847/1538-4357/ac0cef](https://doi.org/10.3847/1538-4357/ac0cef)

Guo, J. H., Ni, Y. W., Zhou, Y. H., et al. 2022, *A&A*, 667, A89, doi: [10.1051/0004-6361/202244253](https://doi.org/10.1051/0004-6361/202244253)

Guo, J. H., Zhou, Y. H., Guo, Y., et al. 2021b, *ApJ*, 920, 131, doi: [10.3847/1538-4357/ac17e8](https://doi.org/10.3847/1538-4357/ac17e8)

Guo, J. H., Ni, Y. W., Guo, Y., et al. 2024a, *ApJ*, 961, 140, doi: [10.3847/1538-4357/ad088d](https://doi.org/10.3847/1538-4357/ad088d)

Guo, J. H., Ni, Y. W., Guo, Y., et al. 2024b, *ApJ*, 961, 140, doi: [10.3847/1538-4357/ad088d](https://doi.org/10.3847/1538-4357/ad088d)

Guo, Y., Démoulin, P., Schmieder, B., et al. 2013, *A&A*, 555, A19, doi: [10.1051/0004-6361/201321229](https://doi.org/10.1051/0004-6361/201321229)

Guo, Y., Schmieder, B., Démoulin, P., et al. 2010, *ApJ*, 714, 343, doi: [10.1088/0004-637X/714/1/343](https://doi.org/10.1088/0004-637X/714/1/343)

Guo, Y., Xia, C., & Keppens, R. 2016a, *ApJ*, 828, 83, doi: [10.3847/0004-637X/828/2/83](https://doi.org/10.3847/0004-637X/828/2/83)

Guo, Y., Xia, C., Keppens, R., Ding, M. D., & Chen, P. F. 2019, *ApJL*, 870, L21, doi: [10.3847/2041-8213/aafabf](https://doi.org/10.3847/2041-8213/aafabf)

Guo, Y., Xia, C., Keppens, R., & Valori, G. 2016b, *ApJ*, 828, 82, doi: [10.3847/0004-637X/828/2/82](https://doi.org/10.3847/0004-637X/828/2/82)

Harvey, J. W., Hill, F., Hubbard, R. P., et al. 1996, *Science*, 272, 1284, doi: [10.1126/science.272.5266.1284](https://doi.org/10.1126/science.272.5266.1284)

Hershaw, J., Foullon, C., Nakariakov, V. M., & Verwichte, E. 2011, *A&A*, 531, A53, doi: [10.1051/0004-6361/2011116750](https://doi.org/10.1051/0004-6361/2011116750)

Jerčić, V., Keppens, R., & Zhou, Y. 2022, *A&A*, 658, A58, doi: [10.1051/0004-6361/202142127](https://doi.org/10.1051/0004-6361/202142127)

Jiang, C., Bian, X., Sun, T., & Feng, X. 2021, *Frontiers in Physics*, 9, 224, doi: [10.3389/fphy.2021.646750](https://doi.org/10.3389/fphy.2021.646750)

Joshi, R., Luna, M., Schmieder, B., Moreno-Insertis, F., & Chandra, R. 2023, *A&A*, 672, A15, doi: [10.1051/0004-6361/202245647](https://doi.org/10.1051/0004-6361/202245647)

Joshi, R., Mandrini, C. H., Chandra, R., et al. 2022, *SoPh*, 297, 81, doi: [10.1007/s11207-022-02021-5](https://doi.org/10.1007/s11207-022-02021-5)

Karki, G., Schmieder, B., Démoulin, P., et al. 2025, *SoPh*, 300, 98, doi: [10.1007/s11207-025-02509-w](https://doi.org/10.1007/s11207-025-02509-w)

Karpen, J. T., Antiochos, S. K., & Klimchuk, J. A. 2006, *ApJ*, 637, 531, doi: [10.1086/498237](https://doi.org/10.1086/498237)

Karpen, J. T., Antiochos, S. K., Klimchuk, J. A., & MacNeice, P. J. 2003, *ApJ*, 593, 1187, doi: [10.1086/376690](https://doi.org/10.1086/376690)

Keppens, R., Zhou, Y., & Xia, C. 2025, *Living Reviews in Solar Physics*, 22, 4, doi: [10.1007/s41116-025-00043-2](https://doi.org/10.1007/s41116-025-00043-2)

Kliem, B., & Török, T. 2006a, *PhRvL*, 96, 255002, doi: [10.1103/PhysRevLett.96.255002](https://doi.org/10.1103/PhysRevLett.96.255002)

Kliem, B., & Török, T. 2006b, *PhRvL*, 96, 255002, doi: [10.1103/PhysRevLett.96.255002](https://doi.org/10.1103/PhysRevLett.96.255002)

Kosugi, T., Matsuzaki, K., Sakao, T., et al. 2007, *SoPh*, 243, 3, doi: [10.1007/s11207-007-9014-6](https://doi.org/10.1007/s11207-007-9014-6)

Labrosse, N., Heinzel, P., Vial, J. C., et al. 2010, *SSRv*, 151, 243, doi: [10.1007/s11214-010-9630-6](https://doi.org/10.1007/s11214-010-9630-6)

Lemen, J. R., Title, A. M., Akin, D. J., et al. 2012, *SoPh*, 275, 17, doi: [10.1007/s11207-011-9776-8](https://doi.org/10.1007/s11207-011-9776-8)

Li, H., Guo, J., Cheng, X., et al. 2025, *ApJL*, 979, L46, doi: [10.3847/2041-8213/ada893](https://doi.org/10.3847/2041-8213/ada893)

Li, H. T., Cheng, X., Guo, J. H., et al. 2022, *A&A*, 663, A127, doi: [10.1051/0004-6361/202243115](https://doi.org/10.1051/0004-6361/202243115)

Liakh, V., & Jenkins, J. 2025, *SoPh*, 300, 147, doi: [10.1007/s11207-025-02552-7](https://doi.org/10.1007/s11207-025-02552-7)

Lin, Y., Engvold, O., der Voort, L. R. v., Wiik, J. E., & Berger, T. E. 2005, *SoPh*, 226, 239, doi: [10.1007/s11207-005-6876-3](https://doi.org/10.1007/s11207-005-6876-3)

Liu, Q., & Xia, C. 2022, *ApJL*, 934, L9, doi: [10.3847/2041-8213/ac80c6](https://doi.org/10.3847/2041-8213/ac80c6)

López Ariste, A., Aulanier, G., Schmieder, B., & Sainz Dalda, A. 2006, *A&A*, 456, 725, doi: [10.1051/0004-6361:20064923](https://doi.org/10.1051/0004-6361:20064923)

Luna, M., Karpen, J., Ballester, J. L., et al. 2018, *ApJS*, 236, 35, doi: [10.3847/1538-4365/aabde7](https://doi.org/10.3847/1538-4365/aabde7)

Luna, M., Karpen, J. T., & DeVore, C. R. 2012, *ApJ*, 746, 30, doi: [10.1088/0004-637X/746/1/30](https://doi.org/10.1088/0004-637X/746/1/30)

Luna, M., Mérou Mestre, J. R., & Auchère, F. 2022, *A&A*, 666, A195, doi: [10.1051/0004-6361/202244181](https://doi.org/10.1051/0004-6361/202244181)

Mackay, D. H., Karpen, J. T., Ballester, J. L., Schmieder, B., & Aulanier, G. 2010, *SSRv*, 151, 333, doi: [10.1007/s11214-010-9628-0](https://doi.org/10.1007/s11214-010-9628-0)

Martin, S. F. 1998, *SoPh*, 182, 107, doi: [10.1023/A:1005026814076](https://doi.org/10.1023/A:1005026814076)

Martin, S. F., Marquette, W. H., & Bilimoria, R. 1992, in *Astronomical Society of the Pacific Conference Series*, Vol. 27, *The Solar Cycle*, ed. K. L. Harvey, 53

Mazumder, R., Pant, V., Luna, M., & Banerjee, D. 2020, *A&A*, 633, A12, doi: [10.1051/0004-6361/201936453](https://doi.org/10.1051/0004-6361/201936453)

Mein, P., & Rayrole, J. 1985, *Vistas in Astronomy*, 28, 567, doi: [10.1016/0083-6656\(85\)90077-7](https://doi.org/10.1016/0083-6656(85)90077-7)

Ouyang, Y., Chen, P. F., Fan, S. Q., Li, B., & Xu, A. A. 2020, *ApJ*, 894, 64, doi: [10.3847/1538-4357/ab83f9](https://doi.org/10.3847/1538-4357/ab83f9)

Ouyang, Y., Zhou, Y. H., Chen, P. F., & Fang, C. 2017, *ApJ*, 835, 94, doi: [10.3847/1538-4357/835/1/94](https://doi.org/10.3847/1538-4357/835/1/94)

Pesnell, W. D., Thompson, B. J., & Chamberlin, P. C. 2012, *SoPh*, 275, 3, doi: [10.1007/s11207-011-9841-3](https://doi.org/10.1007/s11207-011-9841-3)

Priest, E. R., & Démoulin, P. 1995, *J. Geophys. Res.*, 100, 23443, doi: [10.1029/95JA02740](https://doi.org/10.1029/95JA02740)

Schmieder, B., Bommier, V., & Gelly, B. 2025, *Universe*, 11, 153, doi: [10.3390/universe11050153](https://doi.org/10.3390/universe11050153)

Schmieder, B., Guo, J., & Poedts, S. 2024, *Reviews of Modern Plasma Physics*, 8, 27, doi: [10.1007/s41614-024-00166-3](https://doi.org/10.1007/s41614-024-00166-3)

Schmieder, B., Malherbe, J. M., & Raadu, M. A. 1985, *A&A*, 142, 249

Schmieder, B., Roudier, T., Mein, N., et al. 2014, *A&A*, 564, A104, doi: [10.1051/0004-6361/201322861](https://doi.org/10.1051/0004-6361/201322861)

Schou, J., Scherrer, P. H., Bush, R. I., et al. 2012, *SoPh*, 275, 229, doi: [10.1007/s11207-011-9842-2](https://doi.org/10.1007/s11207-011-9842-2)

Shen, Y., Liu, Y. D., Chen, P. F., & Ichimoto, K. 2014, *ApJ*, 795, 130, doi: [10.1088/0004-637X/795/2/130](https://doi.org/10.1088/0004-637X/795/2/130)

Tan, S., Shen, Y., Zhou, X., et al. 2023, *MNRAS*, 520, 3080, doi: [10.1093/mnras/stad295](https://doi.org/10.1093/mnras/stad295)

Tandberg-Hanssen, E. 1974, *Solar Prominences*, Vol. 12

Tandberg-Hanssen, E. 1995, *Science*, 269, 111

Titov, V. S., Downs, C., Mikić, Z., et al. 2018, *ApJL*, 852, L21, doi: [10.3847/2041-8213/aaa3da](https://doi.org/10.3847/2041-8213/aaa3da)

Tsuneta, S., Ichimoto, K., Katsukawa, Y., et al. 2008, *SoPh*, 249, 167, doi: [10.1007/s11207-008-9174-z](https://doi.org/10.1007/s11207-008-9174-z)

van Ballegooijen, A. A. 2004, *ApJ*, 612, 519, doi: [10.1086/422512](https://doi.org/10.1086/422512)

van Ballegooijen, A. A., & Martens, P. C. H. 1989, *ApJ*, 343, 971, doi: [10.1086/167766](https://doi.org/10.1086/167766)

Wang, W., Liu, R., Qiu, J., Guo, J., & Wang, Y. 2025, *ApJ*, 982, 115, doi: [10.3847/1538-4357/adb7d8](https://doi.org/10.3847/1538-4357/adb7d8)

Wiegelmann, T., & Neukirch, T. 2006, *A&A*, 457, 1053, doi: [10.1051/0004-6361:20065281](https://doi.org/10.1051/0004-6361:20065281)

Xia, C., Chen, P. F., Keppens, R., & van Marle, A. J. 2011, *ApJ*, 737, 27, doi: [10.1088/0004-637X/737/1/27](https://doi.org/10.1088/0004-637X/737/1/27)

Xia, C., Keppens, R., Antolin, P., & Porth, O. 2014, *ApJL*, 792, L38, doi: [10.1088/2041-8205/792/2/L38](https://doi.org/10.1088/2041-8205/792/2/L38)

Xia, C., Teunissen, J., El Mellah, I., Chané, E., & Keppens, R. 2018, *ApJS*, 234, 30, doi: [10.3847/1538-4365/aaa6c8](https://doi.org/10.3847/1538-4365/aaa6c8)

Xing, C., Aulanier, G., Cheng, X., Xia, C., & Ding, M. 2024, *ApJ*, 966, 70, doi: [10.3847/1538-4357/ad2ea9](https://doi.org/10.3847/1538-4357/ad2ea9)

Zhang, Q. M., Li, T., Zheng, R. S., Su, Y. N., & Ji, H. S. 2017, *ApJ*, 842, 27, doi: [10.3847/1538-4357/aa73d2](https://doi.org/10.3847/1538-4357/aa73d2)

Zhang, X. M., Guo, J. H., Guo, Y., Ding, M. D., & Keppens, R. 2024, *ApJ*, 961, 145, doi: [10.3847/1538-4357/ad1521](https://doi.org/10.3847/1538-4357/ad1521)

Zhou, C., Xia, C., & Shen, Y. 2021, *A&A*, 647, A112, doi: [10.1051/0004-6361/202039558](https://doi.org/10.1051/0004-6361/202039558)

Zhou, Y. 2025, *Reviews of Modern Plasma Physics*, 9, 32, doi: [10.1007/s41614-025-00206-6](https://doi.org/10.1007/s41614-025-00206-6)

Zhou, Y. H., Chen, P. F., Hong, J., & Fang, C. 2020, *Nature Astronomy*, 4, 994, doi: [10.1038/s41550-020-1094-3](https://doi.org/10.1038/s41550-020-1094-3)

Zhou, Y.-H., Chen, P.-F., Zhang, Q.-M., & Fang, C. 2014, *Research in Astronomy and Astrophysics*, 14, 581, doi: [10.1088/1674-4527/14/5/007](https://doi.org/10.1088/1674-4527/14/5/007)

Zhou, Y.-H., Zhang, L.-Y., Ouyang, Y., Chen, P. F., & Fang, C. 2017, *ApJ*, 839, 9, doi: [10.3847/1538-4357/aa67de](https://doi.org/10.3847/1538-4357/aa67de)